Intranasal inhibitor broadly blocks SARS-CoV-2 including recent highly immunoevasive Omicron subvariants

Anna R. Mäkelä[1], Hasan Uğurlu[1], Liina Hannula[2], Ravi Kant[1,3], Petja Salminen[1], Riku Fagerlund[1], Sanna Mäki[1], Anu Haveri[4], Tomas Strandin[1], Lauri Kareinen[1,3], Jussi Hepojoki[1], Suvi Kuivanen[1], Lev Levanov[1], Arja Pasternack[5], Rauno A. Naves[5], Olli Ritvos[5], Pamela Österlund[4], Tarja Sironen[1,3], Olli Vapalahti[1,3,7], Anja Kipar[3,6], Juha T. Huiskonen[2], Ilona Rissanen[2] and Kalle Saksela[1,7]

[1] Department of Virology, University of Helsinki, Helsinki, Finland

[2] Institute of Biotechnology, Helsinki Institute of Life Science HiLIFE, University of Helsinki, Helsinki, Finland.

[3] Department of Basic Veterinary Sciences, University of Helsinki, Helsinki, Finland

[4] Finnish Institute for Health and Welfare, Helsinki, Finland.

[5] Department of Physiology, University of Helsinki, Helsinki, Finland

[6] Laboratory for Animal Model Pathology, Institute of Veterinary Pathology, Vetsuisse Faculty, University of Zurich, Zurich, Switzerland

[7] HUS Diagnostic Centre, HUSLAB, Clinical Microbiology, Helsinki University Hospital, Helsinki, Finland.

* Correspondence: kalle.saksela@helsinki.fi

SUMMARY

The recent emergence of novel SARS-CoV-2 variants capable of efficiently escaping neutralizing antibodies emphasizes the need for prophylactic strategies to complement vaccination in fighting the COVID-19 pandemic. Nasal epithelium is rich in the ACE2 receptor and important for SARS-CoV-2 transmission by supporting early viral replication before seeding to the lung[1]. Intranasal administration of SARS-CoV-2 neutralizing antibodies or antibody fragments has shown encouraging potential as a protective measure in animal models[2-5]. However, there remains a dire need for SARS-CoV-2 blocking agents that are less vulnerable to mutational variation in the neutralization epitopes of the viral spike glycoprotein and more economical to produce in large scale. Here we describe TriSb92, a highly manufacturable and extremely stable trimeric human SH3 domain-derived antibody mimetic targeted against a conserved region in the receptor-binding domain of spike. TriSb92 potently neutralizes SARS-CoV-2 and its variants of concern, including Omicron BA.5 as well as the latest and most immunoevasive variants like BF.7, XBB, and BQ.1.1. Intranasal administration of a modest dose of TriSb92 (5 or 50 micrograms) as early as eight hours before a challenge with SARS-CoV-2 efficiently protected mice from infection, and was still effective even when given 4 h after the viral challenge. The target epitope of TriSb92 was defined by cryo-EM, which revealed triggering of a conformational shift in the spike trimer rather than competition for ACE2 binding as the molecular basis of its strong inhibitory action. The high potency and robust biochemical properties of TriSb92 together with the remarkable resistance of its inhibitory action against viral sequence evolution suggest that TriSb92 could be useful as a nasal spray for protecting susceptible individuals from SARS-CoV-2 infection.

48 **INTRODUCTION**

49 The success of the current vaccines in the fight against the SARS-CoV-2 pandemic is challenged by
50 the emergence of novel viral variants of concern (VOCs) that show striking resistance to neutralizing
51 antibodies induced by vaccinations or prior infection. Moreover, immune disorders or other health
52 conditions can preclude appropriate vaccine responses in many individuals. In addition to
53 pharmaceuticals for treating COVID-19 disease, new approaches for preventing transmission and
54 spreading of SARS-CoV-2 are therefore urgently needed.

55 Since the nasal epithelium of the respiratory tract is the first dominant replication site of SARS-
56 CoV-2 preceding virus transport into the lung[1], intranasal administration of SARS-CoV-2
57 neutralizing agents poses an attractive prophylactic concept. In animal models, monoclonal
58 antibodies targeted against the spike envelope protein of SARS-CoV-2 have shown to be effective
59 for COVID-19 prophylaxis[6, 7]. To avoid mutational escape from neutralization, such antibodies have
60 been used as cocktails and targeted against conserved regions of spike[8]. Markedly increased potency
61 could also be achieved by constructing a pentameric IgM version of spike-targeted IgG antibodies[4].

62 To develop more economical and manufacturable anti-SARS-CoV-2 reagents, many
63 laboratories have moved from monoclonal antibodies to smaller antibody fragments, including single
64 variable domain-based nanobodies. Several of these have shown promising antiviral efficacy in cell
65 culture or animal models, including utility as an intranasal SARS-CoV-2 prophylaxis[9-12].

66 Compared to these, small antibody-mimetic scaffold proteins are even more robust, versatile to
67 engineer, and cheaper to produce for diverse biological targeting purposes[13]. Sherpabodies (SH3
68 Recombinant Protein Affinity) are very small (< 60 aa) targeting modules that constitute a novel
69 addition to the toolbox of scaffold targeting proteins and comprise of an improved SH3-domain fold
70 derived from the human ciliary adaptor protein nephrocystin[14]. Here, we report engineering of a
71 sherpabody targeted against a highly conserved region in the spike receptor binding domain (RBD)
72 into a potent prophylactic anti-SARS-CoV-2 agent.

73 **RESULTS**

74 **Development of sherpabody-based SARS-CoV-2 inhibitors**

75 With the aim of developing a novel class of inhibitory proteins that could be used for neutralizing
76 SARS-CoV-2, we screened a large antibody-mimetic phage library displaying ~10^{11} unique
77 sherpabodies (Fig. 1A and B) by using the receptor binding domain (RBD) of the spike glycoprotein
78 of the Wuhan-Hu-1 strain as an affinity bait. Starting from the second round of affinity selection and

phage amplification (panning), a clear enrichment of RBD-binding clones was observed. After three panning cycles, 192 individual sherpabody-displaying phage clones were isolated and found to represent 15 different sequences. These 15 unique sherpabodies were tested in phage-ELISA for binding to RBD-mFc, control mFc, or a monoclonal antibody against the E-tag peptide used for monitoring sherpabody display efficiency (see Fig. 1B). All 15 sherpabody clones mediated strong and apparently specific RBD binding (Fig. 1C). Clone number 92 (Sb92) was among the strongest RBD binders and was chosen for further development due to its ability to also bind to RBD of SARS-CoV-1 (see later), suggesting a conserved target epitope that would be unlikely to vary between different variants of SARS-CoV-2. Sb92 was produced as a GST-fusion protein in bacteria and its RBD-binding affinity was evaluated using a semi-quantitative antigen capture-ELISA (Fig. 1D), which indicated an affinity (K_D) of 30 nM.

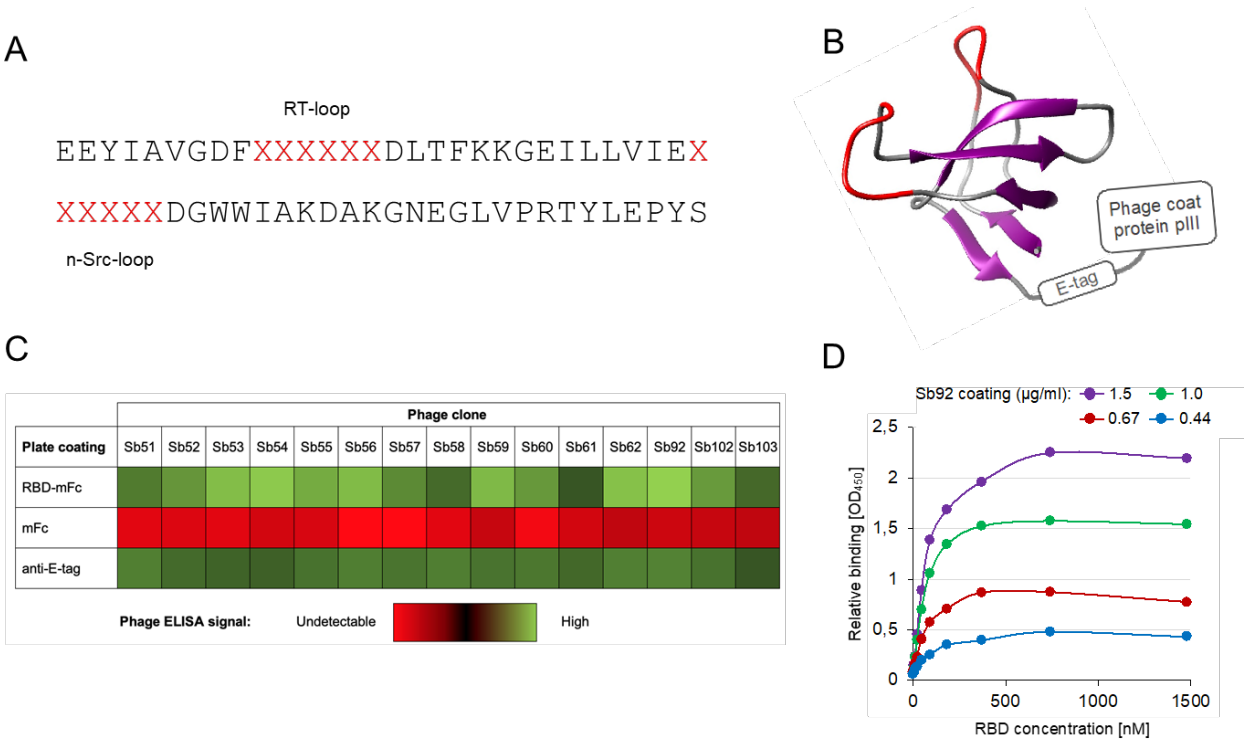

Fig. 1: Discovery of RBD-targeting sherpabodies. (A-B) Six and three residues in the RT- and n-Src-loops, respectively, of the human nephrocystin SH3 domain were replaced with hexapeptides (in red) comprising random combinations of the 20 natural amino acids to create a large semisynthetic M13 phage library displaying ~10^{11} individual sherpabodies with unique binding surfaces formed by the 12 randomized loop residues shown red in the illustration based on the structure pdb 1S1N[14]. **(C)** Heat map showing relative binding in an ELISA assay of fifteen affinity-selected sherpabody-displaying phage clones targeted to RBD of SARS-CoV-2 spike protein (RBD-mFc), negative control (mFc), or an antibody evenly recognizing all displayed clones (anti-E-tag). **(D)** Semi-quantitative ELISA-based analysis of the RBD-binding affinity (30 nM) of the sherpabody clone Sb92.

101 **Neutralization of SARS-CoV-2 and SARS-CoV-1 by trimerized Sb92**

102 To enhance targeting of the trimeric cell surface spike protein we constructed a multimerized
103 derivative of Sb92 (TriSb92) containing three tandem copies of Sb92 connected by flexible 15-mer
104 Gly-Ser linkers. To evaluate the potency of TriSb92 as a neutralizing agent we incubated different
105 viral isolates with serial dilutions of it before infection of VeroE6-TMPRSS2-H10 cultures. When
106 the original Wuhan strain of SARS-CoV-2 was tested a dose-dependent decrease in the number of
107 infected cells was observed corresponding to an impressive IC_{50} value of 0.24 nM (Fig. 2). When
108 clinical SARS-CoV-2 isolates representing the Beta (B.1.351), Delta (B.1.617.2), and Omicron
109 (B.1.1.529) BA.1 variants of concern were tested we observed an even more potent neutralization by
110 TriSb92, resulting in IC_{50} values of 0.11 nM (Beta), 0.18 nM (Delta), and 0.08 nM (BA.1). Finally,
111 we tested also a more recent viral isolate corresponding to the Omicron BA.5 variant that carries
112 several additional mutations in the RBD of its spike protein that provide it with a problematic capacity
113 for evading neutralizing antibody responses. We noted that despite being slightly more resistant than
114 the older variants tested, Omicron BA.5 could also be efficiently neutralized by TriSb92 with a very
115 pleasing IC_{50} value of 0.82 nM.

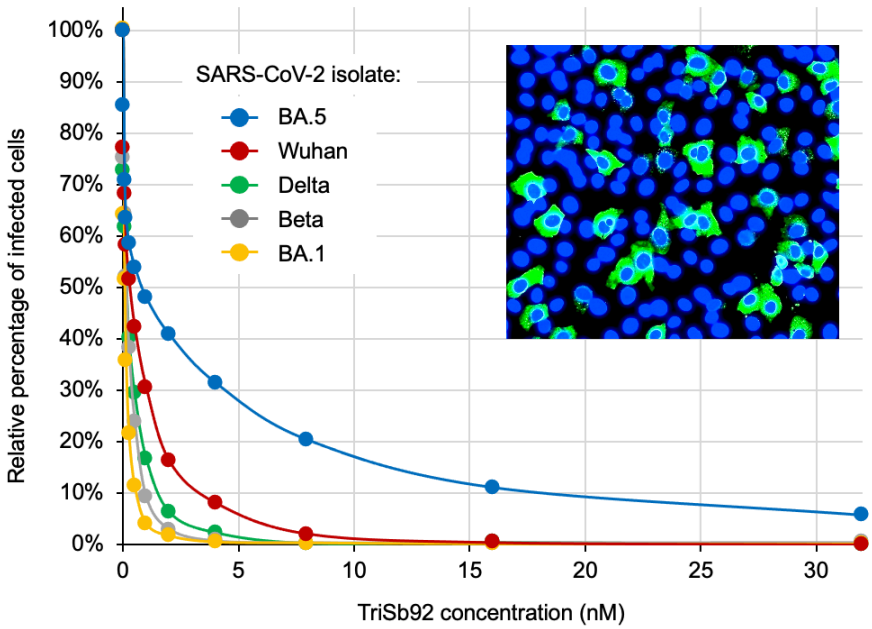

	IC_{50} (nM)
Authentic viruses	
Wuhan	0.24 ±0.06
Beta	0.11 ±0.04
Delta	0.18 ±0.05
BA.1	0.08 ±0.01
BA.5	0.82 ±0.24
Pseudoviruses	
Wuhan	0.06 ±0.02
Beta	0.03 ±0.01
Delta	0.06 ±0.04
BA.1	0.11 ±0.03
BA.3	0.03 ±0.01
BA.2	0.25 ±0.04
BA.2.13	0.19 ±0.10
BA.4/5	0.35 ±0.04
BA.2.3.20	0.08 ±0.01
BF.7	0.18 ±0.03
BQ.1.1	1.74 ±0.30
XBB	1.19 ±0.49
BU.1	0.82 ±0.03
SARS-CoV-1	5.65 ±0.25

116

117 **Fig. 2: Neutralization of SARS-CoV-2 and SARS-CoV-1 by TriSb92.** Half-maximal inhibitory
118 concentration (IC_{50}) of TriSb92 against different authentic SARS-CoV-2 variants or pseudoviruses using the
119 indicated spike proteins were established based on automated counting of fluorescently labelled infected cells
120 (see figure insert) or luciferase reporter gene expression, respectively. Standard deviation for the calculated
121 IC_{50} values is shown. An alignment of RBD sequences of spike variants used in this study is shown in Fig S1.

122

123 To extend these studies to a wider panel of viruses, we utilized a pseudovirus model based on
124 luciferase expressing lentiviral vectors infecting ACE2-expressing HEK293T cells in a spike-
125 dependent manner[15]. Testing of Wuhan, Beta, Delta, Omicron BA.1 and BA.5 spike proteins in this
126 model showed that pseudoviruses are slightly more sensitive to neutralization by TriSb92, but gave
127 results that correlated well with our data on the corresponding authentic SARS-CoV-2 strains (Fig.
128 2). The IC_{50} values derived from these experiments (0.06 nM for Wuhan, 0.03 nM for Beta, 0.06 nM
129 for Delta, 0.11 nM for Omicron BA.1, and 0.35 nM for Omicron BA.5) thus both support our data
130 from using live viruses and help to validate this pseudovirus model for studying the inhibitory potency
131 of TriSb92 against additional virus strains.

132 Recently several new BA.5 subvariants with even higher immunoevasive capacity and ability to
133 escape from neutralization by the currently available therapeutic antibodies have been reported to
134 gain prevalence.[16] To test the potency of TriSb92 against such challenging SARS-CoV-2 strains we
135 generated pseudoviruses carrying spike proteins from a panel of viruses that have emerged and caused
136 concern around the world in mid- and late-2022 (Fig. 2 and Fig. S1). All these pseudoviruses could
137 also be efficiently neutralized by TriSb92, although the IC_{50} values had increased from the
138 subnanomolar range to 1-2 nM. Finally, we created a pseudovirus based on the spike glycoprotein of
139 SARS-CoV-1, and found that it could also be readily neutralized by TriSb92, albeit with a somewhat
140 lower efficiency (IC_{50} 5.65 nM) than the SARS-CoV-2 variants tested (Fig. 2).

141 Together, these data show that TriSb92 is a potent inhibitor of SARS-CoV-2 infection, which targets
142 a conserved site in the RBD of spike in a manner that is insensitive to mutations found in the older as
143 well as the currently prevalent and emerging SARS-CoV-2 variants, and provides TriSb92 with a
144 capacity to neutralize a related sarbecovirus (SARS-CoV-1).

145 **TriSb92 induces a conformational change in the S2 subunit of the spike protein**

146 To understand the mechanism behind the potent SARS-CoV-2 neutralization by TriSb92 we
147 examined whether it inhibited attachment of spike-dependent pseudovirus particles to target cells. To
148 this end, these virions were either untreated or treated for 30 min with 100 ng/ml of TriSb92 (a
149 concentration sufficient to fully suppress infectivity) or a high-titre COVID-19 convalescent serum
150 before incubation with ACE2-expressing HEK293 cells, followed by washing of unbound virions
151 and Western blot analysis of lysates of these cells for the p24 pseudoviral capsid protein. We found
152 that treatment with TriSb92 did not affect target cell binding of the spike-pseudotyped virions,
153 whereas this was completely blocked by the convalescent serum used as a control (Figure 3A).

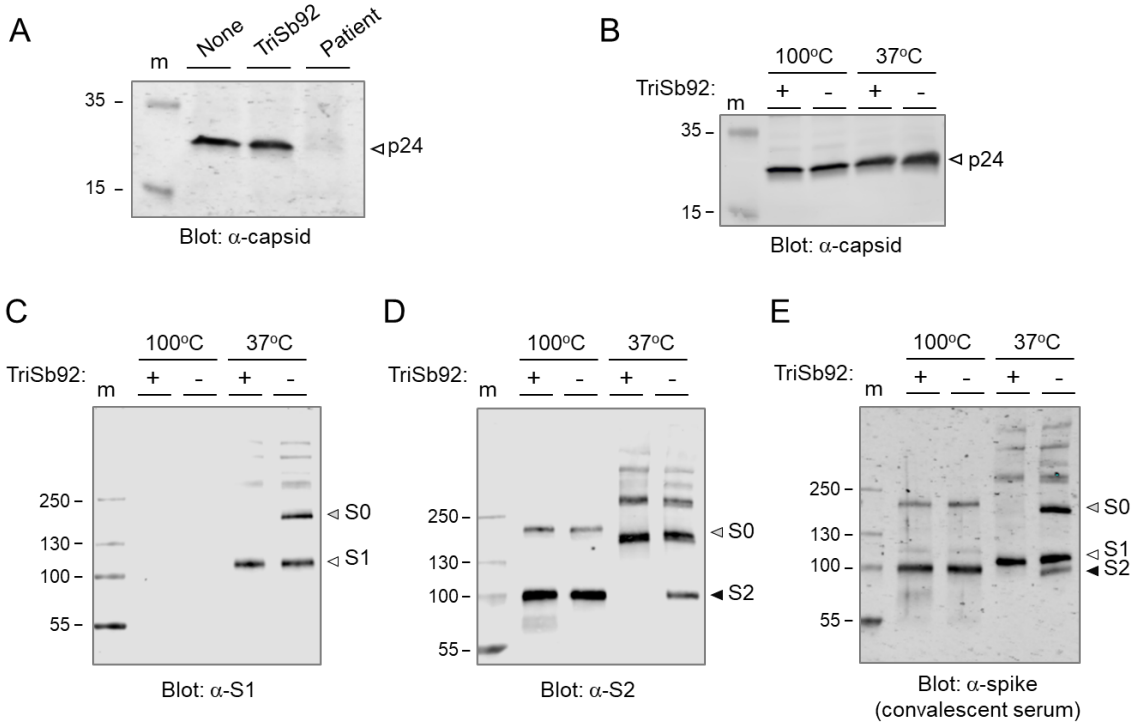

Fig. 3: TriSb92 does not prevent virus attachment to target cells but prevents infection by inducing a conformational change in spike. (A). Spike-decorated pseudoviruses were treated with TriSb92, COVID-19 convalescent serum (Patient), or left untreated (None) before incubated with ACE2-expressing HEK293 cells. The amount cell-associated pseudoviral capsid protein (p24) after washing of the cultures was determined by Western blotting. (**B-E).** Spike-pseudotyped virions treated (+) or not treated (-) with TriSb92 were lysed in SDS-PAGE loading buffer and warmed (37ºC) or boiled (100 ºC) before analysed by Western blotting using antibodies specific for the p24 capsid protein (B), spike S1 subunit (C), spike S2 subunit (D), or COVID-19 convalescent serum that can recognize S1 and S2.

While this result ruled out displacement and shedding of the S1 subunit from the spike complex as the principal mechanism of action of TriSb92, it was still of interest to compare the relative amounts of S1 and S2 subunits and uncleaved spike (S0) protein present in TriSb92-treated and untreated virions. Concentrated virus preparations were lysed in SDS-PAGE loading buffer and either warmed to 37ºC or boiled under reducing conditions to help detecting different types of epitopes in Western blots, which were probed with polyclonal rabbit sera specific for S1 or S2, or with the human convalescent serum (Fig. 3C-E).

Both the rabbit anti-S1 and the human anti-spike sera were able to detect S1 only if the samples had not been boiled. Use of these antibodies clearly showed that the amount of virion-associated S1 was not affected by TriSb92 treatment, thus further ruling out S1 shedding as the inhibitory mechanism

174 of TriSb92. The rabbit anti-S2 and the human anti-spike sera readily detected S2 protein irrespective
175 of the preheating temperature, but stronger S2 signals were obtained after boiling. In the case of the
176 boiled samples TriSb92-treatment had no effect on the amount of S2 detected by these antisera, as
177 one would expect for a membrane-anchored viral protein. However, whereas S2 was detected by both
178 antisera in the unboiled control sample, it could not be seen in the corresponding TriSb92-treated
179 sample. A similarly striking behaviour was observed for the intact spike protein (S0) where the S2
180 subunit remains covalently connected to S1, as the rabbit anti-S1 and the human anti-spike sera could
181 detect S0 only in the unboiled control but not in the TriSb92-treated sample.

182 Based on these observations we conclude that regardless of the proteolytic cleavage status of the
183 spike protein binding of TriSb92 to the RBD of its S1 subunit induces a conformational change in the
184 S2 subunit, which depending on the experimental condition can affect detection of cleaved S2 and
185 the uncleaved S0 precursor in Western blotting.

186 **Intranasally administered TriSb92 provides efficient prophylactic pre- and post-exposure**
187 **protection in mouse models of SARS-CoV-2 infection and disease**

188 To evaluate the prophylactic efficiency of TriSb92 *in vivo*, we used a recently described animal model
189 of COVID-19 where Balb/c mice are intranasally inoculated with the SARS-CoV-2 Beta (B.1.351)
190 variant.[17] At different time points before the SARS-CoV-2 challenge mice received intranasal
191 administration of TriSb92. In the first experiment, mice received 25 μg of TriSb92 per nostril and
192 were challenged intranasally one hour later with $2x10^5$ PFU of SARS-CoV-2 B.1.351. This amount
193 of TriSb92 was chosen to represent a relatively modest dose, which is in the range also referred as
194 ultra-low in the SARS-CoV-2 antibody inhibitor literature[2].

195 Animals were euthanized at 2 days post infection (dpi) and the right lungs subjected to
196 quantitative real-time PCR (RT-qPCR) for viral RNA. In untreated control mice, the lungs exhibited
197 abundant SARS-CoV-2 subgenomic E RNA (median Cq value 18.45), whereas none could be
198 detected in the lungs of the mice that had received a prophylactic dose of TriSb92. These data are
199 shown in Fig. 4A where mouse actin mRNA-normalized sgE RNA quantitation data are plotted as
200 percentage of the average sgRNA in the five unprotected control mice. The results were confirmed
201 by histology and immunohistology for the detection of SARS-CoV-2 nucleoprotein (NP) in nasal
202 mucosa, airways, and left lungs (Fig. 4B). In control animals, viral antigen was present throughout
203 the respiratory tract, in the nasal cavity (respiratory and olfactory epithelial cells), in bronchiolar
204 epithelial cells and in pneumocytes in adjacent alveoli in association with a mild acute
205 bronchointerstitial pneumonia. Viral antigen was also detected within individual macrophages in

206 bronchiolar lymph nodes. In contrast, treated animals were entirely free of viral antigen in nose, lower
207 airways, lungs, and bronchiolar lymph nodes and did not exhibit any pathological changes (Fig. 4B).

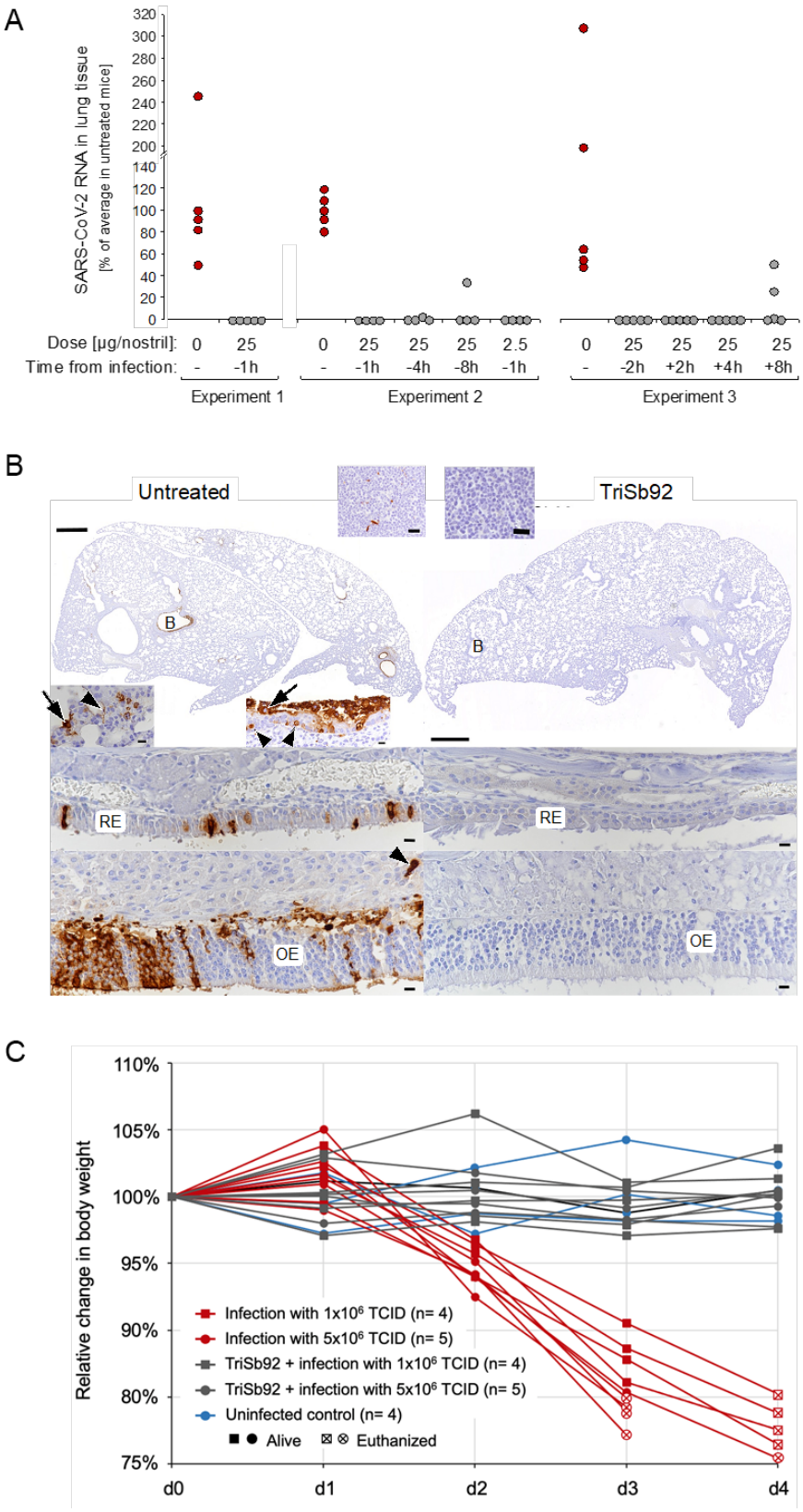

208

Fig. 4. Prophylactic and early therapeutic efficacy of TriSb92 in mice. (A) Subgenomic viral RNA was quantified in lung tissues of Balb/c mice 2 days after challenge with $2x10^5$ PFU of SARS-CoV-2 B.1.351 in three independent infection experiments. The infected mice were treated with intranasal administration TriSb92 at the indicated doses and times before or after the infection. **(B)** SARS-CoV-2 nucleoprotein immunostaining in the nasal cavity and lung tissues 2 days after infection in an untreated mouse (left) and in a mouse pretreated with 25 µg of TriSb92 per nostril (right). The untreated animal exhibits viral antigen expression in the nasal respiratory epithelium (RE) and olfactory epithelium (OE). In the lung, several bronchioles (B) exhibit viral antigen in a variable number of epithelial cells that are often degenerate (arrowheads) or sloughed off (arrows). In infected alveoli, both type I pneumocytes (arrowhead) and type II pneumocytes (arrow) are positive. The bronchial lymph node (top inset) exhibits several positive cells (macrophages or dendritic cells). The animal that received TriSb92 does not exhibit any evidence of viral antigen expression in nasal epithelium, lung and bronchial lymph node. Bars: lung overviews – 500 µm; bronchial lymph nodes – 20 µm; all others – 10 µm. **(C)** Body weight development of Balb/c mice that were infected with $1x10^6$ or $5x10^6$ PFU of the pathogenic SARS-CoV-2 strain maVie16 following intranasal administration TriSb92 (25 µg of per nostril; red lines and symbols) or the same volume of saline buffer (grey lines and symbols) 1h earlier, as indicated. Four control mice received similar mock treatment but no TriSb92 or virus (blue lines and symbols). The experiment was terminated at day 4 post-infection when all infected mice that had not received TriSb92 prophylaxis had been euthanized because of losing 15% or more of their weight (crossed empty symbols).

In a second larger experiment, the protective effect of the previously used dose of TriSb92 was compared with a 10-fold lower dose (2.5 µg per nostril) similarly administered 1 h before SARS-CoV-2 challenge. In addition, we tested the effect of the 25 µg per nostril administered 4 h or 8 h before virus inoculation. As shown in Fig. 4A, also the lower dose of TriSb92 efficiently protected the animals from subsequent SARS-CoV-2 challenge 1 h later (no detectable sgE RNA in lungs 3 days postinfection); however, in two of these animals viral antigen was detected in a few patches of bronchiolar epithelial cells. Remarkably, TriSb92 was very effective also when given 4 h before the viral challenge. None of these animals showed evidence of viral antigen expression in the lung, and in only one of the four animals low but detectable levels of sgE RNA were found. Likewise, when TriSb92 was given 8 h before the challenge the lungs of 3 of the 4 mice were clean of sgE RNA and viral antigen, whereas one animal did show substantial albeit reduced viral RNA levels and also expressed viral antigen within bronchiolar epithelial cells.

A third experiment was carried out to examine the early therapeutic potency of TriSb92 when administered after SARS-CoV-2 infection of epithelial cells had already occurred. The same dosing of 25 µg of TriSb92 per nostril and a challenge with $2x10^5$ PFU of SARS-CoV-2 B.1.351 were again used. The results on the five unprotected animals recapitulated our earlier data, showing abundant sgE RNA in the lungs together with widespread viral antigen expression in the bronchiolar and

246 alveolar epithelium (Table S2), whereas no sgE RNA or viral antigen could be detected in any of the
247 five control mice that received a prophylactic TriSb92 treatment 2 h before the challenge.

248 Strikingly, close to complete lack of sgE RNA in the lungs was also observed at 2 days after the high-
249 dose SARS-CoV-2 challenge when TriSb92 was administered 2 h or even 4 h after the infection (Fig
250 4A). No Cq value for sgE RNA could be obtained for 4 of the 5 animals treated 4 h post-infection,
251 while Cq 32,66 was measured for one animal (indicating sgE RNA levels < 0.01% of the average in
252 the five untreated mice). TriSb92 given 8 h after SARS-CoV-2 was still very beneficial, although an
253 efficient suppression of viral sgE RNA expression in the lungs could be seen only in 3/5 of the mice
254 (undetectable in two, 1.3% of untreated in one). Perhaps due to the initial establishment of the
255 infection, however, the mice treated with TriSb92 after the infection were not equally devoid of viral
256 antigen in their lungs compared to the mice that received TriSb92 prophylactically. SARS-CoV-2
257 nucleoprotein could be detected in the same cell types, although being markedly less widespread and
258 extensive than in the untreated animals (see Table S2). Moreover, whereas in the untreated mice the
259 infection of the bronchiolar epithelium was associated with degenerative changes, no such
260 pathological alterations were observed in mice treated post-infection with TriSb92.

261 To extend these studies to an animal model involving more severe disease pathogenesis we used the
262 mouse-adapted SARS-CoV-2 virus maVie16 that induces profound disease and mortality in BALB/c
263 mice recapitulating many aspects of human COVID-19.[18] Also of note, in resemblance to the recently
264 emerged immunoevasive Omicron variant derivatives (such as BJ.1, BA.2.82, BH.1) the spike protein
265 of maVie16 has acquired mutations affecting the RBD residues K417, Q493, and Q498. We used a
266 lower ($1x10^6$ TCID) or a higher ($5x10^6$ TCID) dose of maVie16 to infect two groups of nine Balb/c
267 mice, half of which had received TriSb92 intranasally (25 µg/per nostril) one hour earlier, and then
268 monitored possible disease progression by daily body weight recording (Fig 4C). Four mice that
269 received just mock treatment but no TriSb92 or virus were included as controls and likewise
270 monitored. All nine infected animals that did not receive TriSb92 experienced significant weight loss
271 at day 2, which at day 3 was so severe (≥15%) that 3 of 4 mice in the higher viral dose group and at
272 day 4 all of the remaining 6 control mice had to be euthanized. By contrast, none of the mice that
273 received a prophylactic dose of TriSb92 showed any signs of weight loss (Fig 4C) or could be
274 distinguished from the uninfected control animal based on their apparent well-being or behaviour.

275 Together, these data show that in these two animal models intranasal administration of TriSb92 at
276 relatively low doses can provide an impressive protection and postexposure prophylactic effect

277 against SARS-CoV-2 infection as measured by virological and histopathological parameters as well
278 as objective severity of disease progression.

279 **Feasibility of TriSb92 for use as a prophylactic formulation**

280 To assess the feasibility of formulating TriSb92 into an intranasal spray or drop for human use, we
281 examined some of its key properties in this regard, namely *in vitro* toxicity, potential cross-reactivity
282 against nasal epithelium, and stability under relevant storage temperatures. The results of these
283 studies were impressive. More specifically, even when applied at very high concentration (1000
284 µg/ml) to human primary endothelial cell (hNECs) culture, TriSb92 caused no signs of reduced cell
285 viability, as analyzed by measuring cellular metabolic activity (Fig. S2). When binding of TriSb92 to
286 extracts of hNECs was tested in an ELISA-like assay, no signal above the background of the assay
287 was seen with any of the tested TriSb92 concentrations (as high as 10 µg/ml), whereas a strong
288 binding signal was observed from extracts prepared from the same cells transduced to express SARS-
289 CoV-2 RBD (Fig. S3). Finally, we did not observe any loss of neutralizing activity of TriSb92
290 obtained from our research grade purification protocol and stored in PBS with no added preservatives
291 or inhibitors up to 15 months in ultra-low freezer (-80ºC), regular freezer (-20ºC), refrigerator (+4ºC),
292 or at room temperature (+20-25ºC) (Fig. S4).

293 **TriSb92 targets a conserved region in the RBD**

294 To gain structural and mechanistic insight into the broadly cross-neutralizing action of TriSb92,
295 cryogenic electron microscopy (cryoEM) studies were carried out. Single-particle cryoEM analysis
296 of the prefusion SARS-CoV-2 S trimer mixed with TriSb92 resulted in two reconstructions with
297 average estimated resolutions of 2.9 Å and 3.1 Å (Fig. S5, Fig. S6 and Table S1; 6–7Å resolution
298 over the flexible RBD regions) that display the distinct "up" and "down" conformations characteristic
299 of sarbecoviral RBDs[19-21]. The first reconstruction, A, describes the S-trimer with all three RBDs in
300 the up-conformation decorated with additional density corresponding to bound TriSb92 (Fig. 5A).
301 The second reconstruction, B, describes the S-trimer with all three RBDs in the down-conformation
302 without any additional density indicative of a sherpabody (Fig. S5). To corroborate that the additional
303 density associated with the up-conformation RBDs was TriSb92-derived, we generated a model of
304 Sb92 with I-TASSER[22] and fitted it into the additional density, confirming that this density perfectly
305 matched with the size and shape of the SH3-fold of TriSb92 (Fig. S7). The placement of RBD and
306 Sb92 models was unambiguous at map resolution of 6.9 Å, and identified the RT-loop of Sb92 as a
307 key mediator of Sb-RBD interactions (Fig. S7).

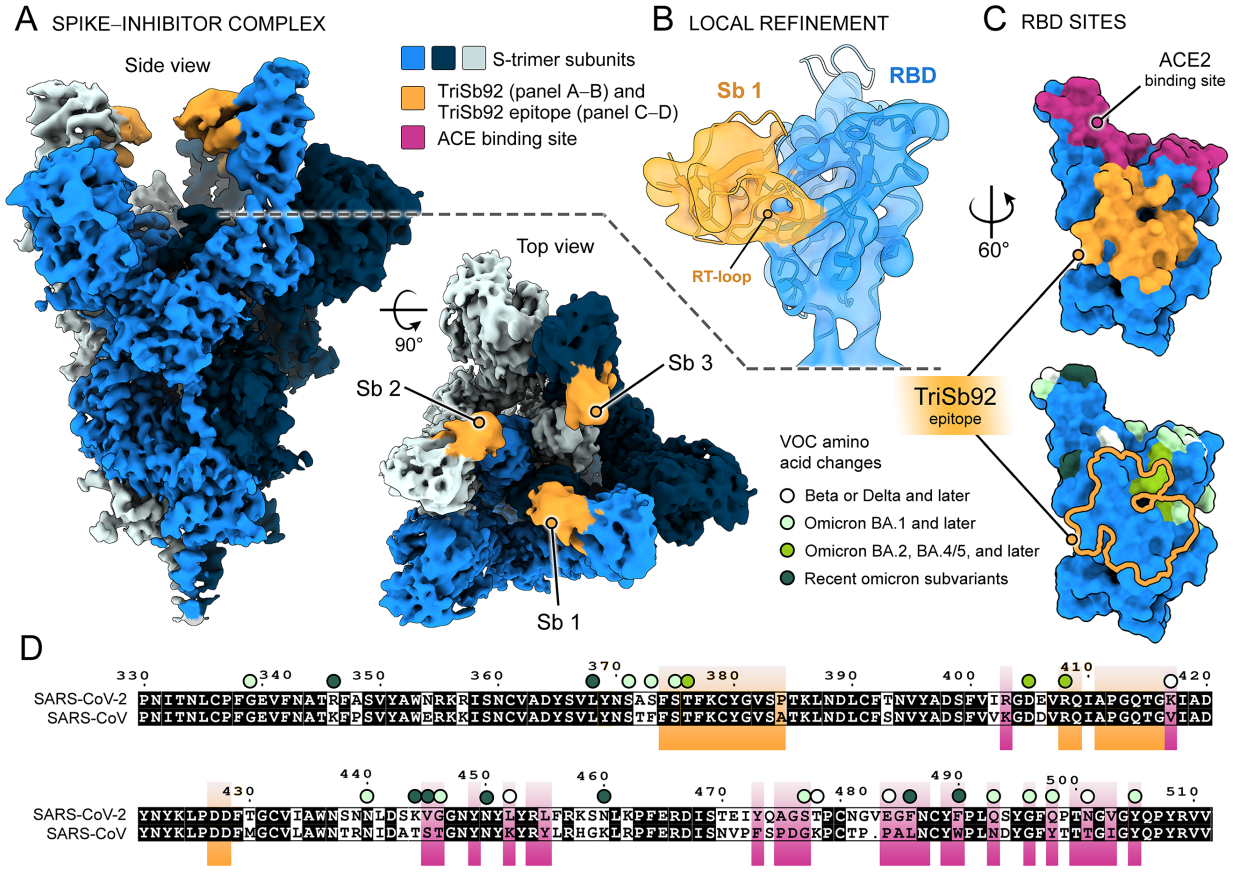

Fig. 5: Cryo-EM of SARS-CoV-2 S in complex with TriSb92 reveals the highly conserved TriSb92 binding site. (A) Side and top views of the cryoEM reconstruction of spike trimer in complex with TriSb92. **(B)** Locally refined cryoEM reconstruction of the RBD region, with fitted models of Sb92 (generated with I-TASSER) and the RBD (PDB 7KMS). **(C)** Surface rendering of the RBD with ACE2 binding site and the TriSb92 epitope highlighted (upper panel), and the location of amino acid changes in VOCs relative to the TriSb92 epitope highlighted (lower panel) **(D)** Pairwise sequence alignment of SARS-CoV-1 and SARS-CoV-2. The binding sites of TriSb92 and ACE2 are highlighted in orange and in purple, respectively. Circles above the RBD residues indicate amino acid changes in Omicron, Delta, and/or Beta variants, and are coloured as follows: white is found in Beta or Delta and later (Omicron) variants; mint green is found in Omicron BA.1 and later subvariants; medium lime green is found in Omicron BA.2, BA.4/5; dark green is found in the most recent Omicron subvariants. The mapped amino acid changes and associated variant information are presented in Fig. S1.

As illustrated in Figs. 5C-D, TriSb92 targets a highly conserved region distal from the ACE2 binding site. In line with the observed cross-neutralization (Fig. 2), only a single residue within the predicted binding site of TriSb92 diverges between SARS-CoV-2 (Wuhan-Hu-1) and SARS-CoV-1. On the other hand, apart from just three of the 27 RBD amino acids changes subsequently acquired by SARS-CoV-2 (S375F, T376A and R408S, which are located at the very edge of the TriSb92 epitope) these VOCs, including the most recent Omicron subvariants do not contain mutations involving this

328 binding surface (Fig. 5C-D). The epitope of TriSb92 is distinct from the epitopes of therapeutic
329 monoclonal antibodies (Fig. S8) that primarily target the ACE2 binding site and remain vulnerable
330 to amino acid changes accruing in this region. Instead, the epitope of TriSb92 partially overlaps with
331 the 'cryptic epitope' targeted by monoclonal antibody (mAb) CR3022[23] (Fig. S8) that does not
332 compete with binding to ACE2. Indeed, the ability of ACE2 and Sb92 to simultaneously bind to the
333 RBD in a non-competitive manner could also be experimentally verified using a sandwich-ELISA
334 approach (Fig. S9).

335

336 **DISCUSSION**

337 The emergence of new SARS-CoV-2 variants that compromise vaccine efficacy and are resistant to
338 the available therapeutic monoclonal antibodies[24-29] underscores the importance to develop novel
339 molecular tools that potently neutralize VOCs. In this study, we describe a promising SARS-CoV-2
340 inhibitor, TriSb92, based on a new and extremely small antibody-mimetic targeting scaffold termed
341 the sherpabody. TriSb92 targets a highly conserved region and could neutralize all tested VOCs and
342 even a related sarbecovirus SARS-CoV-1.

343 In our hands the pseudoviruses were slightly more sensitive to neutralization than the corresponding
344 authentic SARS-CoV-2 variants, but in both cases the concentration of TriSb92 required for half-
345 maximal inhibition of infection (IC_{50}) was less than 300 pM for all pre-Omicron SARS-CoV-2
346 variants as well as for Omicron BA.1 and BA.3, where only one amino acid change (S375F) appears
347 within the TriSb92 epitope. Evolution from BA.1 to the BA.2 and BA.5 lineages resulted in two
348 additional RBD amino acid changes (T376A and R408S) located in the periphery of the TriSb92-
349 binding interface, which was associated with a modest decrease in sensitivity to TriSb92.
350 Nevertheless, BA.5 was still very effectively neutralized by TriSb92 with a subnanomolar IC_{50} value
351 measured for a clinical isolate (0.82 nM) as well as a corresponding pseudovirus (0.35 nM). Some of
352 the more recent Omicron variants (BF.7, BA.2.13, and BA.2.3.20) were equally or even more
353 sensitive compared to BA.5, whereas others (BU.1, XBB, and BQ.1.1) were 2- to 5-fold less sensitive
354 to the TriSb92. None of these newer variants contain additional amino changes in the TriSb92 binding
355 region (see Figure S9). Considering that the mechanism of action of TriSb92, discussed below, it
356 could be speculated that mutations elsewhere in the S gene may have provided increased stability for
357 the pre-fusion conformation of spike proteins encoded by some of the recent BA.5 subvariants.

358 In any case, all of the tested variants, including XBB, and BQ.1.1 were potently neutralized by
359 TriSb92. This suggests that TriSb92 is likely to be effective also against future immune escape

360 variants of SARS-CoV-2, and considering the high conservation of the TriSb92 target epitope in
361 related animal viruses, it could also be useful as a first line of defence against emerging new pandemic
362 human sarbecoviruses.

363 An advantage of sherpabodies over conventional antibodies and most antibody fragments is that they
364 can be readily assembled into multimers in a context-independent manner to enhance avidity,
365 specificity, as well as functionality. The trimeric design of TriSb92 was chosen considering the
366 trimeric architecture of the SARS-CoV-2 spike glycoprotein. This provided TriSb92 an impressive
367 capacity for half-maximal inhibition (IC_{50}) of the SARS-CoV-2 infection at picomolar concentration
368 despite only a moderately high binding affinity (K_D) of 30 nM of the interaction between a monomeric
369 Sb92 sherpabody and an individual RBD (Wuhan-Hu-1).

370 Besides its binding avidity, the strong neutralization potency of the trimeric TriSb92 inhibitor may
371 also to stem from its mode of action. Instead of competing with the high-affinity interaction between
372 ACE2 and the RBD of spike, TriSb92 prevents SARS-CoV-2 entry by triggering a conformational
373 change in the spike trimer. Our cryo-EM results show that engagement with TriSb92 induces an "all
374 three RBDs up" state of spike. Interestingly, the binding site of TriSb92 is inaccessible in the down-
375 conformation of the RBD. We postulate that once an RBD of the spike samples the up-conformation
376 (the common "one RBD up" state), a subunit of TriSb92 binds to the RBD, and the remaining two
377 free TriSb92 subunits readily sequester ensuing up-conformations of the two other RBDs until an all-
378 up conformation is achieved. This model is consistent with our findings that following TriSb92
379 treatment, the S-trimer presents primarily in an all-up state (~54%) fully engaged with the
380 sherpabody, with smaller populations of mixed up/down and all-down states (Fig. S6). However, the
381 "all three RBDs up" state observed in our cryoEM analysis, performed using a prefusion-stabilized
382 (K986P/V987P mutations) spike ectodomain with an abrogated furin cleavage site and a C-terminal
383 trimerization domain, appears to reflect only the initial stage of this inhibitory conformational change,
384 which in the case of native spike trimer on the viral membrane results in a more fundamental structural
385 reorganization. Treatment of spike-decorated pseudoviral particles with TriSb92 induced an altered
386 conformation in the S2 subunit of spike that was evidenced by a failure to detect cleaved S2 or S2-
387 containing S0 precursor protein by Western blotting. Instead, the amount of virion-associated cleaved
388 S1 protein remained unchanged, indicating that TriSb92 treatment did not lead to shedding of the S1
389 subunit, as has been demonstrated for certain antibodies that target RBD epitopes overlapping with
390 the TriSb92 binding region[30, 31]. In agreement, we also did not observe any decrease in virion
391 attachment to ACE2 receptor-expressing target cells by TriSb92. Thus, we conclude that the
392 inhibitory mechanism of TriSb92 involves pushing of virion-associated spike from its native

393 prefusion state into a bona fide post-fusion or another conformation that cannot support productive
394 viral entry after receptor binding.

395 TriSb92 was built from a sherpabody clone (Sb92) derived from phage-library screening without any
396 further affinity optimization. Thus, it should be relatively facile to achieve an even higher inhibitory
397 potency by affinity maturation of Sb92 and perhaps also by optimization of the trimerization linkers
398 in TriSb92. However, this may not be of great practical relevance considering the already low IC_{50}
399 concentrations of TriSb92 and the ease of producing it in very high quantities in low-cost bacterial
400 expression systems. Moreover, the remarkable on-shelf stability in ambient temperatures render
401 TriSb92 a suitable candidate for nasal spray products.

402 Treatment of mice intranasally with as little as 5 ug of TriSb92 could effectively protect them from a
403 subsequent challenge with SARS-CoV-2. The intranasal dose of TriSb92 that should be administered
404 to susceptible persons at risk for SARS-CoV-2 exposure remains to be established but is likely to be
405 substantially lower than extrapolation of our current data on mice that were challenged by inoculation
406 of a rather massive amount of SARS-CoV-2 ($2x10^5$ TCID of B.1.351 or $5x10^6$ of maVie16) into their
407 respiratory tract. Likewise, compared to the current mouse model data the time window allowed for
408 administering TriSb92 before or after natural SARS-CoV-2 exposure to prevent active viral
409 replication and disease could be wider. Moreover, even in cases when TriSb92 would fail to prevent
410 the infection from progressing, by limiting the early amplification of the virus in the epithelium of
411 the nasal cavity and nasopharynx and thereby delaying the infectious process TriSb92 could
412 effectively tip the balance in favour of the host and thereby help to reduce the risk of severe COVID-
413 19 disease.

414 The pressure on healthcare systems posed by the continuously emerging new viral variants
415 emphasizes the need for new innovations to tackle the rapidly evolving immune escape potential of
416 SARS-CoV-2, and to prepare for future pandemics caused by related sarbecoviruses evolving in the
417 nature. Our current data show that TriSb92 represents a valuable addition to the arsenal of available
418 measures for addressing these challenges.

419 **MATERIALS AND METHDOS**

420 **Phage panning**

421 Sherpabody phage display library (size ~10^{11} cfu) was obtained from Next Biomed Therapies Oy. To
422 develop sherpabodies specific for SARS-CoV-2 spike receptor binding domain (RBD), phage affinity
423 selection process was conducted using standard solid phase sorting strategy. Specific phage-displayed
424 sherpabodies were selected for by panning against RBD-mouse IgG2a Fc-fusion protein[32]. Three
425 sequential rounds of off-target depletion and specific panning were performed using a control mFc
426 and specific RBD-mFc, respectively. The immobilized control and target proteins (30 µg/ml in PBS;
427 Maxisorp Immunotubes, Nunc) were sequentially incubated in the presence of infectious naïve
428 sherpabody phage library in 2.5% milk-PBS-0.1%Tween20, for 2 h (RT) and o/n (4°C), respectively.
429 Non-specific phages were removed by extensive washing (PBS-0.05% PBS-Tween), and the
430 remaining pool of phage were eluted and amplified in *E.coli* XL1-Blue host cells according to
431 standard protocols. The amplified pool of phages was collected, and the process was reiterated over
432 three rounds to enrich phage-displayed sherpabodies specific to the RBD-target protein.

433 **Screening and characterization of RBD-binding clones by ELISA**

434 Representative transformants from the second and third panning rounds were tested for specific
435 binding to the RBD-mFc target protein by enzyme-linked immunosorbent assay (ELISA). Mimicking
436 the affinity selection process, in phage-ELISA the target and control proteins were immobilized on
437 an immunoplate (Maxisorp, Nunc). Each single colony represents progeny from a single *E. coli* cell
438 that harbours a phagemid expressing a unique sherpabody-pIII fusion protein. Specifcally, phage-
439 ELISA was performed in 96-well Maxisorp microtiter plates (Nunc) coated over night at 4°C with
440 100 µl of target and control proteins (10 µg/ml in PBS). The wells were washed 3 x with PBS-0.05%
441 Tween20 and blocked with 5% skimmed milk powder in PBS (milk-PBS) for 2 h at RT. Appropriate
442 dilutions of sherpabody-displaying single phage clones were prepared in milk-PBS and incubated
443 with the coated target protein for 1 h at RT followed by washes 3 x with PBS-0.05% Tween20 to
444 remove unbound phage. The detection was performed with HRP-conjugated mouse monoclonal anti-
445 M13 antibody (GE Healthcare), and TMB (3,3' 5,5'-tetramethylbenzidine) substrate. The staining
446 reaction was stopped with 1 M sulfuric acid and absorbance measured at 450 nm using Hidex Sense
447 Microplate Reader.

448 The DNA encapsulated by the positive phage clones was then sequenced and translated to determine
449 the sequence of the displayed sherpabody.

450 **Sherpabody production and purification**

451 The discovered unique sherpabodies were cloned and expressed in *E. coli* as monomeric and/or
452 trimeric GST-fusion proteins using standard protocols (GE Healthcare). 15 mer Gly-Ser, $(GGGGS)_3$,
453 linkers were applied in between each fusion partner. GST-tagged sherpabodies were purified by
454 affinity chromatography using glutathione sepharose according to manufacturer's instructions (GE
455 Healthcare). The buffer was exchanged to PBS by dialysis (140 mM NaCl, 10 mM phosphate buffer,
456 3 mM KCl, pH 7.4), and the purified sherpabodies were stored at -80°C, -20°C and/or at +4°C.

457 **ELISA**

458 Affinity analysis by semi-quantitative sandwich-ELISA was performed using plastic-coated (o/n,
459 4°C) GST-sherpabody fusion protein followed by binding of a concentration series of soluble RBD-
460 His target protein[32] (1 h, RT). The washes and detection was performed as described above using
461 monoclonal HRP-conjugated anti-His antibody.

462 GST-Sb92/RBD-His/ACE2-mFc sandwich-ELISAs were performed in two ways: first using plastic-
463 coated GST-Sb92 as the capturing reagent (10 µg/ml) and ACE2-mIgG2a as the detection reagent
464 (10 µg/ml) and then vice-versa (10 µg/ml and 5 µg/ml, respectively) to analyse their ability to
465 simultaneously bind to RBD-His[32] (2-fold dilution series starting from 10 µg/ml). The complex
466 formation was detected using either HRP-conjugated goat anti-Mouse-IgG (Sigma Aldrich) or mouse
467 monoclonal anti-GST (GE Healthcare) antibodies. Her2-binding GST-Sb1206 served as a negative
468 control.

469 The specificity (off-target) of TriSb92 binding to RBD was investigated by ELISA. Whole cell lysates
470 of primary human nasal epithelial cells (HNECs; see isolation protocol below) were prepared by
471 lysing 10^6 cells/ml in ice cold Lysis buffer (50 mM Tris pH 7.4, 150 mM NaCl, 1% NP-40, 1 mM
472 EDTA) for 30 min, on ice (vortexing every 5-10 min). Nunc Maxisorp 96-well plates were coated
473 with the concentrated cell lysates o/n, +4°C (100 µl/well, 1:100 in PBS). Whole cell lysate derived
474 from HNECs transduced with an adenoviral vector directing the expression of cell-surface expressed
475 RBD of SARS-CoV-2 spike protein were used as a positive control. The ELISA was performed
476 similarly as described above using standard protocols.

477 **Neutralization assays**

478 HEK293T and HEK293T-ACE2 cells were maintained in DMEM supplemented with 10% fetal
479 bovine serum, 2% L-Glutamine, and 1% penicillin/streptomycin (complete medium). Angiotensin-
480 converting enzyme 2 (ACE2) expressing HEK293T cells were generated by lentivirus-mediated gene
481 transduction. Briefly, pWPI-puro plasmid containing ACE2 cDNA (AB046569.1) was co-transfected
482 with p8.9NdSB and vesicular stomatitis virus G protein (VSV-G) expressing envelope plasmids into
483 HEK293T cells in complete medium using polyethylenimine. The recombinant lentivirus containing
484 supernatant was collected 48 h post-transfection, filtered and used to infect wild-type HEK293T cells.
485 Transduced cells were selected with puromycin.

486 Luciferase encoding SARS-CoV-2 pseudotyped reporter virus was generated by transfecting
487 HEK293T cells with p8.9NdSB, pWPI-GFP expressing Renilla luciferase, and pCAGGS, an
488 expression vector containing the SARS-CoV-2 S protein cDNA of the Wuhan-Hu-1 reference strain
489 (NC_045512.2). The last 18 amino acids containing an endoplasmic reticulum (ER)-retention signal
490 of the spike protein was removed to enhance transport to the plasma membrane. SARS-CoV-1
491 pseudovirus was similarly constructed. Pseudovirus stocks were harvested 48 hours after transfection,
492 filtered and stored at -80°C. Inserts for the pseudotyping expression vectors producing spike
493 glycoproteins encoded by the original Wuhan-Hu-1 strain (with D614G mutation) or its variants
494 B.1.351 (Beta), B.1.617.2 (Delta), and B.1.1.529 (Omicron), including the subvariants BA.1, BA.3,
495 BA.2, BA.2.13, BA.4/5, BA.2.3.20, BF.7, BQ.1.1, XBB, BU.1, or SARS-CoV-1 were assembled
496 from synthetic DNA fragments (Integrated DNA Technologies) using Gibson assembly cloning kit
497 (New England Biolabs) and verified by DNA sequencing.

498 To assess its neutralizing activity TriSb92 was serially diluted in complete medium. 12.5 µl of
499 TriSb92 dilutions were mixed with 37.5 µl of luciferase encoding SARS-CoV-2 pseudotyped reporter
500 viruses in 96-well cell culture plates and incubated at 37°C for 30 min. After incubation, 20 000
501 HEK293T-ACE2 cells (in 50 µl) were added to the wells and the plates were further incubated at
502 37°C for 48 h. The amount of internalized pseudovirus in infected cells was quantified by measuring
503 luciferase activity using Renilla-GLO assay (Promega). The relative luciferase units were normalized
504 to those of control samples. Half maximal inhibitory concentrations (IC_{50}) were determined from
505 three parallel experiments.

506 To assess the inhibitory activity of TriSb92 against clinical virus isolates, the neutralization was
507 performed as described above for the pseudoviruses with the following modifications: 40 000
508 VeroE6-TMPRSS2-H10 cells[33] were seeded per well and mixed with virus-inhibitor mixture, which

509 was replaced with complete DMEM 1 h post infection (p.i) at 37°C. Nine hours later the cells were
510 fixed with 4% paraformaldehyde, permeabilized with 3% BSA-PBS-0.3 % Triton-X100, and labelled
511 with rabbit polyclonal anti-SARS-CoV-2 nucleoprotein (NP; produced in-house) primary antibody
512 and goat Alexa Fluor 488-conjugated (Invitrogen) anti-rabbit polyclonal secondary antibody. The cell
513 nuclei were visualized by Hoechst staining, and the percentage of cells that labelled positive for
514 SARS-CoV-2 NP was quantified using Opera Phenix High Content Screening System (PerkinElmer).
515 Each experimental condition involved five replicate wells, and an average of 15,000 cells (total
516 >70,00 per condition) per well were analyzed. The half maximal inhibitory concentrations (IC_{50})
517 were determined from at least two such large experiments.

518 The clinical isolates used in this study were isolated in Finalnd from patient nasopharyngeal samples.
519 Beta variant is the isolate hCoV-19/Finland/THL-202101018/2021 (EPI_ISL_3471851), Delta is
520 hCoV-19/Finland/THL-202117309/2021 (EPI_ISL_2557176), Omicron/BA.1 is hCoV-
521 19/Finland/THL-202126660/2021 (pending for the Gisaid ID), Omicron/BA5.1 is hCoV-
522 19/Finland/THL-202213593/2022 (EPI_ISL_13118918, GeneBank ID OP435368). Viruses were
523 propagated in VeroE6-TMPRSS2-H10 cells[33]. The generation of mouse-adapted maVie16 SARS-
524 CoV-2 is described elsewhere[18].

525 **Cell viability assay**

526 Primary human nasal epithelial cells (HNECs) were isolated by brushing from the nasal cavity of a
527 male donor. The isolated cells were cultured and maintained in PneumaCult™-Ex Plus Basal Medium
528 supplemented with 1x PneumaCult™-Ex Plus Supplement, 1x hydrocortisone (200x stock solution
529 96 µg/ml) and 1x penicillin-streptomycin (all from StemCell Technologies). For cell expansion, the
530 culture flasks and plates were coated with Collagen Solution according to manufacturer's
531 instructions, and Animal Component-Free Cell Dissociation Kit was used for dissociation and
532 passaging (all from StemCell Technologies).

533 For the cell viability assay, HNECs were cultured on an opaque-walled 96-well plate (10 000
534 cells/well) for 24 h, and then treated with a 2-fold concentration series of TriSb92 diluted in complete
535 culture medium (starting from 1 mg/ml) for 24 h at 37°C. NaN_3 (5%) served as a cytotoxic drug
536 control. Cell viability was measured using CellTiter-Glo® 2.0 Assay (Promega) according to
537 manufacturer's instructions. Average and standard deviations of a representative assay performed in
538 triplicates were calculated.

539 **Stability of TriSb92 during long-term on-shelf storage**

The stability of TriSb92 after long-term storage in different temperatures was investigated using pseudovirus neutralization assay using Wuhan-Hu-1 reference strain. TriSb92 was stored as 1 mg/ml stocks in PBS (140 mM NaCl, 10 mM phosphate buffer, 3 mM KCl, pH 7.4) in room temperature [RT; +21-25°C], fridge [+6-8°C] or freezer [-20°C or -80°C] for 1-14 months (mo).

Animal studies

Balb/c mice (Envigo) were transported to the University of Helsinki (Finland) biosafety level 3 (BSL-3) facility and acclimatized to individually ventilated biocontainment cages (ISOcage; Scanbur) for seven days with ad libitum water and food (rodent pellets). After the acclimatization period, 9-week old female Balb/c were placed under isoflurane anesthesia and intranasally inoculated with 25 µl per nostril of TriSb92 (25 or 2.5 µg/nostril). The mice were challenged by infection with 20 µl of SARS-CoV-2 B.1.351 clinical isolate ($2x10^5$ PFU) or with mouse-adapted maVie16 SARS-CoV-2[18] (0.5-$1x10^6$ PFU). Immediately following the inoculation, the isoflurane was switched off and the animals were held in an upright position for a few seconds to allow the liquid to flush downwards in the nasal cavity. All mice were weighed on a daily basis, and their wellbeing was carefully monitored throughout the experiment for signs of illness (changes in posture or behaviour, rough coat, apathy, ataxia and weight loss), but none of the mice showed any clinical signs. Euthanasia was performed 2 days post infection under terminal isoflurane anesthesia with cervical dislocation. All animals were dissected immediately after death and the right lungs collected for virological examination. The left lung, remaining thoracic organs and heads (animals from the first experiment) were fixed in 10% buffered formalin for 48 h and stored in 70% ethanol for histological and immunohistochemical examinations. Experimental procedures were approved by the Animal Experimental Board of Finland (license number ESAVI/28687/2020).

RNA isolation and RT-PCR

RNA was extracted from the right lung of the mice using Trizol (Thermo Scientific) according to the manufacturer's instructions. Isolated RNA was directly subjected to one-step RT-qPCR analysis using TaqMan fast virus 1-step master mix (Thermo Scientific) and AriaMx instrumentation (Agilent) as described previously for E and subE genes[34]. The RT-qPCR for actin was conducted as previously described.[35] Relative quantification of actin-normalized viral RNA levels was achieved by the comparative Ct method[36] using the average of non-treated animals as reference.

571 **Histology and immunohistochemistry**

572 The left lung, remaining thoracic organs and heads were trimmed for histological examination. Heads
573 were sawn longitudinally in the midline using a diamond saw (Exakt 300; Exakt) and gently
574 decalcified in RDF (Biosystems) for 5 days at room temperature and on a shaker. Tissues were
575 routinely paraffin wax embedded. Consecutive sections (3–5 µm) were prepared from lungs and
576 heads and routinely stained with hematoxylin-eosin (HE) or subjected to immunohistochemistry for
577 the detection of SARS-CoV-2 antigen, as previously described[17].

578 **Recombinant SARS-CoV-2 S trimer production and complex formation.**

579 To express the SARS-CoV-2 S, a gene encoding for the prefusion stabilized S protein ectodomain[20]
580 was produced as synthetic cDNA (GeneArt, Life Technologies). The cDNA template encoded for the
581 residues 14−1208 of the original Wuhan-Hu-1 strain S protein (NCBI Reference Sequence:
582 YP_009724390.1) with prefusion-stabilizing proline substitutions at residues 986 and 987, an
583 abrogated furin S1/S2 cleavage site with a "GSAS" substitution at residues 682–685, and a C-terminal
584 T4 fibritin trimerization motif followed by an HRV3C protease cleavage site, SpyTag003, and
585 8xHisTag. The gene was cloned into the mammalian expression vector pHLsec (Adgene) and
586 transfected into Expi293F™ (Thermo Fisher Scientific) suspension cells at a density of 3×10^6 cells
587 per ml using the ExpiFectamine™ 293 Transfection Kit (Thermo Fisher Scientific). Following 6 days
588 of cultivation on an orbital shaker a 36.5°C and 5% CO2, the S protein containing supernatant was
589 collected, clarified by centrifugation, and filtered through a 0.45 µM filter. Imidazole was added to
590 the supernatant to 3 mM final concentration, and SARS-CoV-2 S protein was purified from the
591 supernatant by immobilized nickel affinity chromatography with a 1-ml HisTrap excel column
592 (Cytiva) using 300 mM imidazole for elution. S-protein containing eluate was concentrated and buffer
593 exchanged to 10 mM Tris pH 8 + 150 mM NaCl buffer using an Amicon Ultra centrifugal filter
594 (MWCO 100 kDa, Millipore). Prior to grid preparation, pure TriSb92 was added to a purified S-
595 trimer aliquot at 1.5x molar excess, and the complex was incubated on ice for 15 minutes.

596 **Cryo-EM grid preparation, data acquisition and data processing.**

597 A 3-µl aliquot of a pure, prefusion SARS-CoV-2 S-trimer (0.3 mg/ml) mixed with TriSb92 (0.05
598 mg/ml) was applied on Quantifoil 1.2/1.3 grids (1.2-µm hole diameter, 200 mesh copper) that had
599 been glow discharged in a plasma cleaner (PDC-002-CE, Harrick Plasma) for 30 s. The grids were
600 blotted for 8 s and plunged into liquid ethane using a vitrification apparatus (Vitrobot, Thermo Fisher
601 Scientific). Data were collected on a Titan Krios transmission electron microscope (Thermo Fisher
602 Scientific) equipped with Gatan K2 direct electron detector using electron exposure of 55 $e^-/Å^2$ per

603 image at a nominal magnification of 165,000x, resulting in a pixel size of 0.82 Å (Table S1). Data
604 were processed in cryoSPARC[37](Fig. S6). Contrast transfer function parameters were estimated by
605 CTFFIND4[38]. Particles were picked with Topaz[39], using a subset of S-trimer particles first pruned by
606 2D classification as the training set. After another round of 2D classification to discard false positive
607 particles, an initial volume of the S trimer was calculated ab initio. After 3D refinement of particle
608 poses and shifts, local motion correction, extraction of particles with box size of 512x512 and second
609 round of refinement with C3 symmetry, the symmetry was expanded, and the particles were subjected
610 to 3D variability analysis[40] which focused to the RBD region. This revealed two main classes of
611 particles 'all RBDs up' and 'all RBDs down'. Maps of both classes were reconstructed with non-
612 uniform refinement. A map for 'all RBDs down' (reconstruction B) class was calculated applying C3
613 symmetry, after removing the symmetry copies created by symmetry expansion. For 'all RBDs up'
614 map, no symmetry was applied (reconstruction A). Instead, the RBD region density was further
615 refined by local, focused refinement using particles where the bulk of the S-trimer density had been
616 subtracted. The resulting maps were filtered to local resolution for further analysis. CryoEM data
617 collection and processing statistics are presented in Table S1.

618 **Fitting SARS-CoV-2 S and Sb92s into the cryo-EM reconstructions.** A

619 molecular model of the SARS-CoV-2 S-trimer, derived from PDB 7KMS[41], was docked into our
620 reconstruction A of the SARS-CoV-2 spike using the 'fitmap' function in UCSF ChimeraX[42]. In
621 short, a map was simulated for the S-trimer structure to the resolution of 2.9 Å, to match the resolution
622 of the spike reconstruction, and fitting was performed using fitmap global search. The top solution
623 yielded a map-to-map correlation score of 0.78, confirming that, similar to structure 7KMS, our
624 reconstruction of the S-trimer displays a "3-up" RBD conformation. We observed that the innate
625 flexibility of RBDs resulted in weaker density features in RBD regions of the full spike
626 reconstruction, and so, RBDs were modelled into locally refined RBD-region density (Figs. S6 and
627 S7). First, an RBD was separated from the 7KMS spike structure in Coot[43] and fitted into the locally-
628 refined RBD region reconstruction using fitmap in ChimeraX, yielding a correlation score of 0.86.
629 Furthermore, additional density not comprised of the S-protein was observed adjacent to each RBD
630 (Figure 5). To confirm whether this density was comprised of Sb92, the cryoEM reconstruction was
631 segmented around the RBD using 'color zone' (coloring radius of 2.5Å) and 'split map' functions in
632 Chimera, followed by fitting a model of Sb92, predicted by I-TASSER[22]to high confidence (C-score
633 0.51) and geometry optimized in Phenix[44], into the additional density with a fitmap global search.
634 The top solution placed Sb92 into the density adjacent to RBDs with a correlation score of 0.78.
635 Furthermore, this sherpabody placement reveals that the RT-loop, which contains antigen-binging

636 mutations in Sb92 (Figure 1), forms a key interface with the RBD (Fig. S7). Residues comprising the
637 RT-loop were refined into the density using ISOLDE[45]within ChimeraX. Finally, three copies of the
638 RBD–Sb complex were fitted back into the reconstruction of the full spike (reconstruction A) and
639 connected to the rest of the fitted spike derived from 7KMS in Coot, completing the model of the
640 SARS-CoV-2 spike in complex with Sb92.

641 Our second reconstruction B (Fig. S5), was validated as a closed conformation by fitting a SARS-
642 CoV-2 structure (PDB 6ZP0[46], presenting a "3-down" RBD conformation) into the density. Fitmap
643 global search was performed between a map simulated for structure 6ZP0 at resolution of 3.1 Å, and
644 our cryoEM reconstruction B, yielding a map-to-map correlation score of 0.76 and leaving no
645 unexplained density.

646 **Molecular graphics and protein interface analysis**. Molecular graphics images were generated
647 using PyMOL (The PyMOL Molecular Graphics System, Version 2.4.0a0, Schrödinger, LLC) and
648 [4747]ChimeraX, developed by the Resource for Biocomputing, Visualization, and Informatics at the
649 University of California[42]. Residues comprising the interface of SARS-CoV-2 S with ACE2 receptor
650 and inhibitors, including TriSb92 and therapeutic monoclonal antibodies, were identified using the
651 PDB ePISA server.

652 **Data availability**

653 The cryo-EM density maps of i) SARS-CoV-2 spike with RBDs in the "up"-conformation and
654 decorated with TriSb92 (accession code EMD-16383) and ii) SARS-CoV-2 spike with RBDs in the
655 "down" conformation (EMD-16388) have been deposited in the EMDB at the EBI. Coordinates of
656 the fitted SARS-CoV-2 spike in complex with Sb92 have deposited in the PDB (accession code PDB
657 8C1V). All data generated or analysed during this study are included in the main text and its
658 supplementary information files.

659

660 **Contributions**

661 ARM and KS designed the study and analysed the data. ARM, HU, PS, JH, LL, RF, KS were
662 responsible for the inhibitor development, characterization and validation. AJ, RN and OR produced
663 and purified the recombinant proteins. SM, AH and PÖ performed the studies with the clinical virus
664 isolates. RK, LK, TSt, TSi, OV were involved in the infectious mouse model and animal studies.
665 AK conducted mouse pathology and immunohistochemistry. Structural biology studies were
666 designed, conducted and analyzed by IR, LH and JTH.

Acknowledgements

We thank Virpi Syvälahti for expert technical assistance, Mikael Ritvos for help with recombinant protein production, Giuseppe Balistreri and Ravi Kant Oiha for human nasal epithelial cells and related advice, Michael Hall, Benita Löflund, and Pasi Laurinmäki for support with electron microscopy. The facilities and expertise of the HiLIFE CryoEM unit at the University of Helsinki, a member of Instruct-ERIC Centre Finland, FINStruct, and Biocenter Finland are gratefully acknowledged. The data was collected at the Umeå Core Facility for Electron Microscopy, a node of the Cryo-EM Swedish National Facility, funded by the Knut and Alice Wallenberg, Family Erling Persson and Kempe Foundations, SciLifeLab, Stockholm University and Umeå University. We are grateful for the facilities and expertise provided to us by the FIMM Genomic Center at the University of Helsinki, CSC - IT Center for Science, Finland, and the Histology Laboratory of Institute of Veterinary Pathology at the University of Zurich. This work was supported by the Academy of Finland (grants 336492 to JTH, 342988 to IR, 336490 and 339510 to OV, 336425 and 331787 to KS), EU Horizon 2020 programme (grant 874735 to OV) as well as funding from the Jane and Aatos Erkko Foundation (OV) and the Sakari Alhopuro Foundation (KS).

682 **References**

683

684 1. Hou, Y.J. et al. SARS-CoV-2 reverse genetics reveals a variable infection gradient in the
685 respiratory tract. Cell 182, 429-446 e414 (2020).

686 2. Nambulli, S. et al. Inhalable Nanobody (PiN-21) prevents and treats SARS-CoV-2 infections
687 in Syrian hamsters at ultra-low doses. Sci Adv 7 (2021).

688 3. Huo, J. et al. A potent SARS-CoV-2 neutralising nanobody shows therapeutic efficacy in the
689 Syrian golden hamster model of COVID-19. Nat Commun 12, 5469 (2021).

690 4. Ku, Z. et al. Nasal delivery of an IgM offers broad protection from SARS-CoV-2 variants.
691 Nature 595, 718-723 (2021).

692 5. Wu, X. et al. A potent bispecific nanobody protects hACE2 mice against SARS-CoV-2
693 infection via intranasal administration. Cell Rep 37, 109869 (2021).

694 6. Baum, A. et al. REGN-COV2 antibodies prevent and treat SARS-CoV-2 infection in rhesus
695 macaques and hamsters. Science 370, 1110-1115 (2020).

696 7. Hartman, A.L. et al. SARS-CoV-2 infection of African green monkeys results in mild
697 respiratory disease discernible by PET/CT imaging and shedding of infectious virus from both
698 respiratory and gastrointestinal tracts. PLoS Pathog 16, e1008903 (2020).

699 8. Du, L., Yang, Y. & Zhang, X. Neutralizing antibodies for the prevention and treatment of
700 COVID-19. Cell Mol Immunol 18, 2293-2306 (2021).

701 9. Wrapp, D. et al. Structural basis for potent neutralization of betacoronaviruses by single-
702 domain camelid antibodies. Cell 181, 1004-1015 e1015 (2020).

703 10. Schoof, M. et al. An ultrapotent synthetic nanobody neutralizes SARS-CoV-2 by stabilizing
704 inactive Spike. Science 370, 1473-1479 (2020).

705 11. Xiang, Y. et al. Versatile and multivalent nanobodies efficiently neutralize SARS-CoV-2.
706 Science 370, 1479-1484 (2020).

707 12. Xu, J. et al. Nanobodies from camelid mice and llamas neutralize SARS-CoV-2 variants.
708 Nature 595, 278-282 (2021).

709 13. Simeon, R. & Chen, Z. In vitro-engineered non-antibody protein therapeutics. Protein Cell 9,
710 3-14 (2018).

711 14. le Maire, A. et al. Solution NMR structure of the SH3 domain of human nephrocystin and
712 analysis of a mutation-causing juvenile nephronophthisis. Proteins 59, 347-355 (2005).

713 15. Crawford, K.H.D. et al. Protocol and reagents for pseudotyping lentiviral particles with
714 SARS-CoV-2 spike protein for neutralization assays. Viruses 12 (2020).

715 16. Cao, Y. et al. BA.2.12.1, BA.4 and BA.5 escape antibodies elicited by Omicron infection.
716 Nature 608, 593-602 (2022).

717 17. Kant, R. et al. Common laboratory mice are susceptible to infection with the SARS-CoV-2
718 beta variant. Viruses 13 (2021).

719 18. Gawish, R. et al. ACE2 is the critical in vivo receptor for SARS-CoV-2 in a novel COVID-
720 19 mouse model with TNF- and IFNgamma-driven immunopathology. Elife 11 (2022).

721 19. Shang, J. et al. Structural basis of receptor recognition by SARS-CoV-2. Nature 581, 221-224
722 (2020).

723 20. Walls, A.C. et al. Structure, function, and antigenicity of the SARS-CoV-2 spike glycoprotein.
724 Cell 181, 281-292 e286 (2020).

725 21. Yuan, Y. et al. Cryo-EM structures of MERS-CoV and SARS-CoV spike glycoproteins reveal
726 the dynamic receptor binding domains. Nat Commun 8, 15092 (2017).

727 22. Yang, J. & Zhang, Y. I-TASSER server: new development for protein structure and function
728 predictions. Nucleic Acids Res 43, W174-181 (2015).

729 23. Yuan, M. et al. A highly conserved cryptic epitope in the receptor binding domains of SARS-
730 CoV-2 and SARS-CoV. Science 368, 630-633 (2020).

731 24. Planas, D. et al. Reduced sensitivity of SARS-CoV-2 variant Delta to antibody neutralization.
732 Nature 596, 276-280 (2021).

733 25. Planas, D. et al. Sensitivity of infectious SARS-CoV-2 B.1.1.7 and B.1.351 variants to
734 neutralizing antibodies. Nat Med 27, 917-924 (2021).

735 26. Chen, R.E. et al. In vivo monoclonal antibody efficacy against SARS-CoV-2 variant strains.
736 Nature 596, 103-108 (2021).

737 27. Dong, Y. et al. The way of SARS-CoV-2 vaccine development: success and challenges.
738 Signal Transduct Target Ther 6, 387 (2021).

739 28. Schmidt, F. et al. Plasma neutralization properties of the SARS-CoV-2 Omicron variant.
740 medRxiv (2021).

741 29. Tada, T. et al. Partial resistance of SARS-CoV-2 Delta variants to vaccine-elicited antibodies
742 and convalescent sera. iScience 24, 103341 (2021).

743 30. Li, T. et al. Cross-neutralizing antibodies bind a SARS-CoV-2 cryptic site and resist
744 circulating variants. Nat Commun 12, 5652 (2021).

745 31. Huo, J. et al. Neutralization of SARS-CoV-2 by Destruction of the Prefusion Spike. Cell Host
746 Microbe 28, 445-454 e446 (2020).

747 32. Jalkanen, P. et al. A Combination of N and S Antigens With IgA and IgG Measurement
748 Strengthens the Accuracy of SARS-CoV-2 Serodiagnostics. J Infect Dis 224, 218-228 (2021).

749 33. Rusanen, J. et al. A generic, scalable, and rapid time-resolved forster resonance energy
750 transfer-based assay for antigen detection-SARS-CoV-2 as a proof of concept. mBio 12
751 (2021).

752 34. Dagotto, G. et al. Comparison of subgenomic and total RNA in SARS-CoV-2 challenged
753 rhesus macaques. J Virol (2021).

754 35. Zivcec, M., Safronetz, D., Haddock, E., Feldmann, H. & Ebihara, H. Validation of assays to
755 monitor immune responses in the Syrian golden hamster (Mesocricetus auratus). J Immunol
756 Methods 368, 24-35 (2011).

757 36. Schmittgen, T.D. & Livak, K.J. Analyzing real-time PCR data by the comparative C(T)
758 method. Nat Protoc 3, 1101-1108 (2008).

759 37. Punjani, A., Rubinstein, J.L., Fleet, D.J. & Brubaker, M.A. cryoSPARC: algorithms for rapid
760 unsupervised cryo-EM structure determination. Nat Methods 14, 290-296 (2017).

761 38. Rohou, A. & Grigorieff, N. CTFFIND4: Fast and accurate defocus estimation from electron
762 micrographs. J Struct Biol 192, 216-221 (2015).

763 39. Bepler, T. et al. Positive-unlabeled convolutional neural networks for particle picking in cryo-
764 electron micrographs. Nat Methods 16, 1153-1160 (2019).

765 40. Punjani, A. & Fleet, D.J. 3D variability analysis: Resolving continuous flexibility and discrete
766 heterogeneity from single particle cryo-EM. J Struct Biol 213, 107702 (2021).

767 41. Custodio, T.F. et al. Selection, biophysical and structural analysis of synthetic nanobodies that
768 effectively neutralize SARS-CoV-2. Nat Commun 11, 5588 (2020).

769 42. Pettersen, E.F. et al. UCSF ChimeraX: Structure visualization for researchers, educators, and
770 developers. Protein Sci 30, 70-82 (2021).

771 43. Emsley, P. & Cowtan, K. Coot: model-building tools for molecular graphics. Acta Crystallogr
772 D Biol Crystallogr 60, 2126-2132 (2004).

773 44. Liebschner, D. et al. Macromolecular structure determination using X-rays, neutrons and
774 electrons: recent developments in Phenix. Acta Crystallogr D Struct Biol 75, 861-877 (2019).

775 45. Croll, T.I. ISOLDE: a physically realistic environment for model building into low-resolution
776 electron-density maps. Acta Crystallogr D Struct Biol 74, 519-530 (2018).

777 46. Xiong, X. et al. A thermostable, closed SARS-CoV-2 spike protein trimer. Nat Struct Mol
778 Biol 27, 934-941 (2020).

779 47. Pettersen, E.F. et al. UCSF Chimera--a visualization system for exploratory research and
780 analysis. J Comput Chem 25, 1605-1612 (2004).

781

782 **Supplementary data**

783

784

785

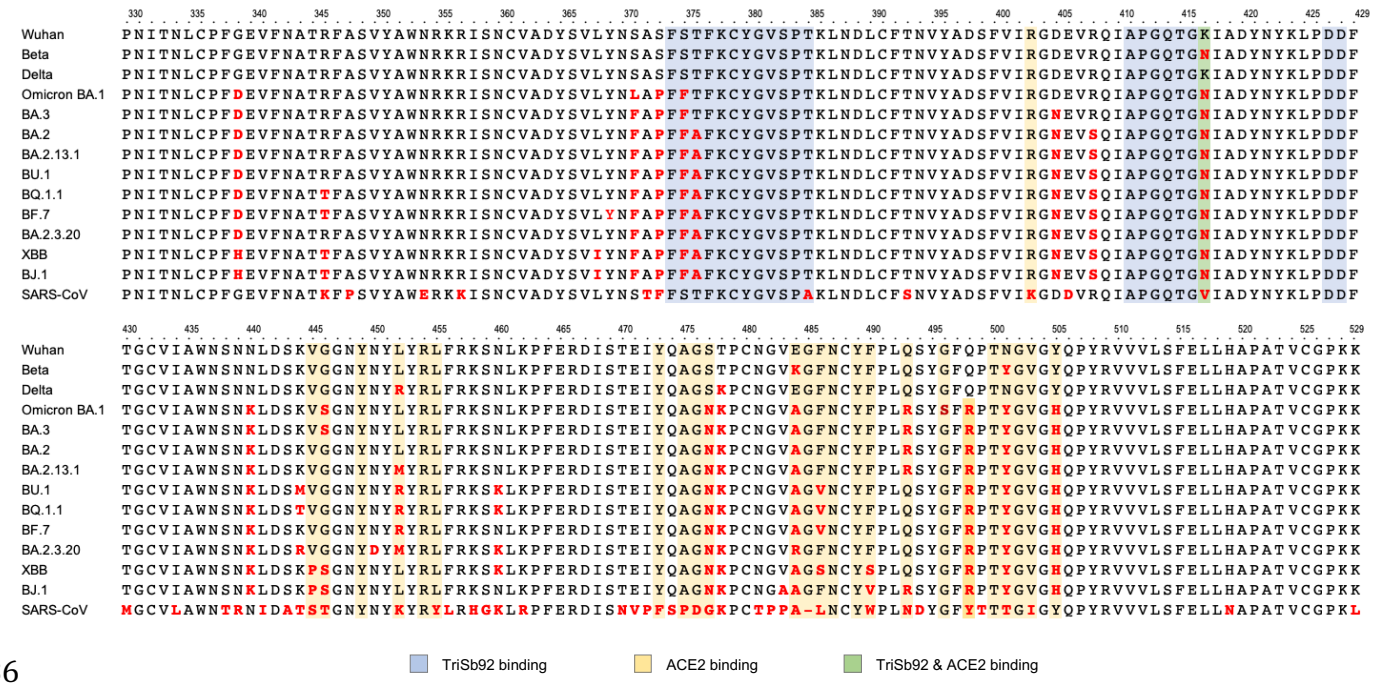

786

787

788 **Supplementary Figure 1: Amino acid alignment of RBD region of SARS-CoV-2 and SARS-**
789 **CoV-1 variants used in this study.** Residues differing from the original SARS-CoV-2 Wuhan strain
790 are indicated in red. Residues involved in the binding interfaces for TriSb92, ACE2, or both are
791 highlighted in blue, yellow, or green, respectively.

792

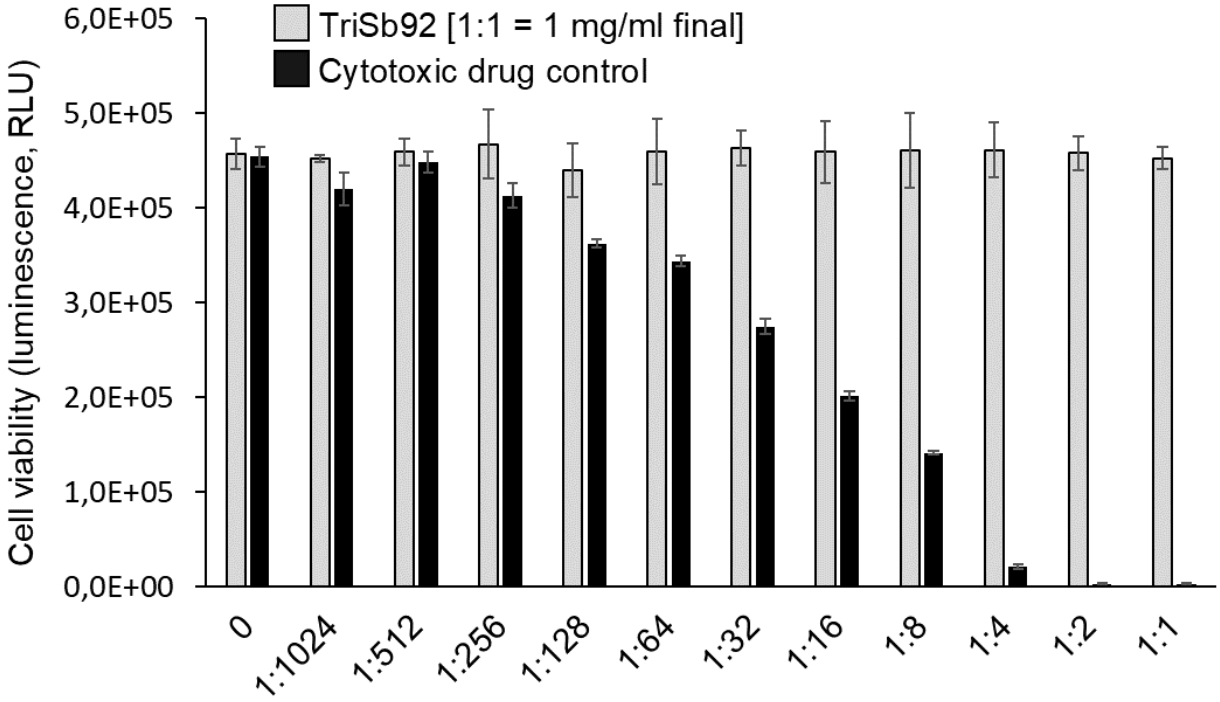

Supplementary Figure 2: TriSb92 shows no cytotoxicity. Viability of primary human nasal epithelial cells treated with increasing concentrations of TriSb92 for 24 h at 37°C. Cellular metabolic activity as a measure of cell viability was monitored using CellTiter-Glo 2.0 assay. Average and standard deviations of a representative assay performed in triplicates is shown.

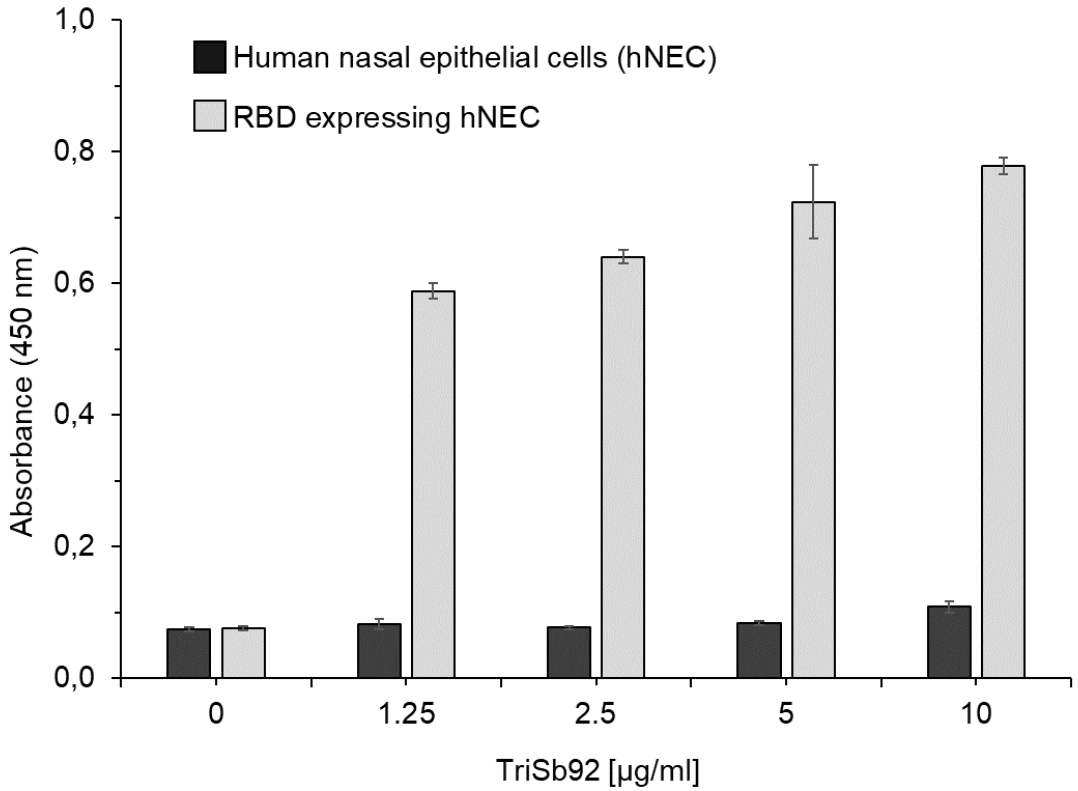

801
802
803
804 **Supplementary Figure 3: Specificity of TriSb92 for RBD and lack of off-target binding to**
805 **primary human nasal epithelial cell (hNECs) proteins.** Binding of increasing concentrations of
806 TriSb92 to hNEC lysates was tested in an ELISA-format. Lysate of the same cells transduced with
807 an adenoviral vector expressing SARS-CoV-2 spike RBD were used as a positive control. Average
808 and standard deviations of a representative assay performed in triplicates is shown.
809
810

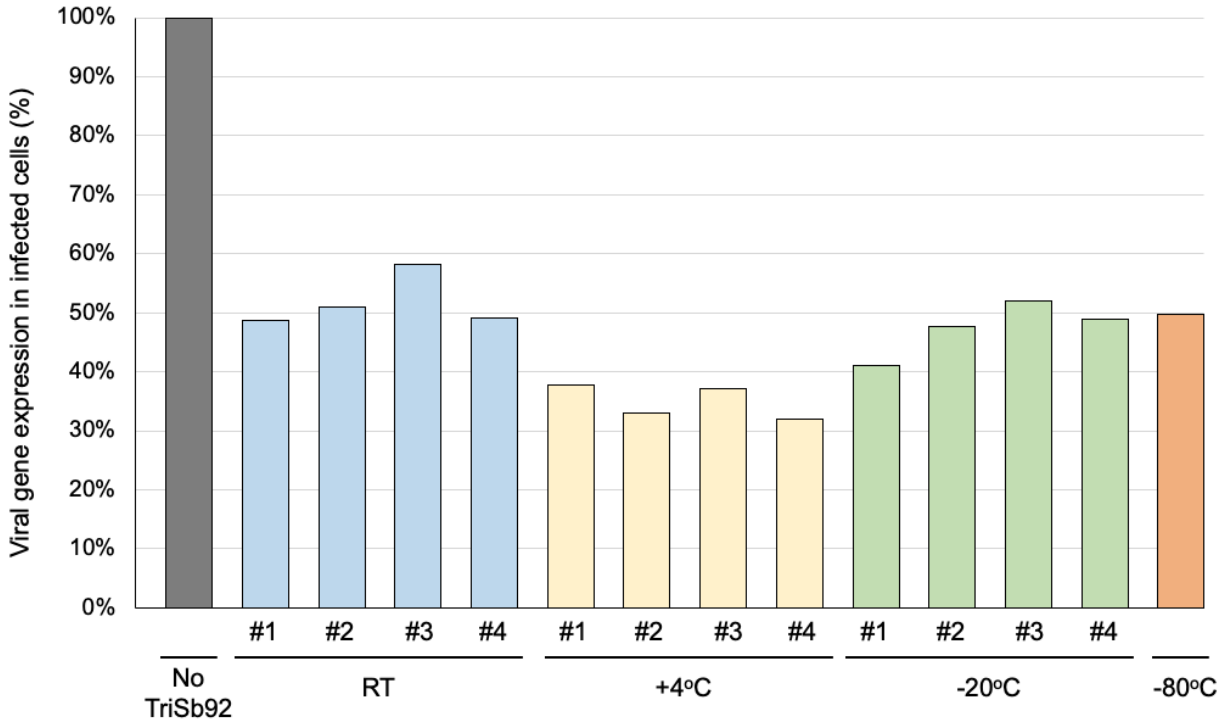

Supplementary Figure 4: Stability analysis of TriSb92 after long-term storage in different temperatures. Four independent aliquots of TriSb92 (1 mg/ml in PBS) stored for 15 months at the indicated temperatures were diluted to the IC_{50} concentration established for Wuhan spike-decorated pseudoviruses (see Fig. 2) and compared for their neutralization activity with TriSb92 stored at -80ºC. The dilutions were prepared based on the originally determined concentration without considering possible decrease in volume due to evaporation of samples stored at room temperature (RT) or +4ºC.

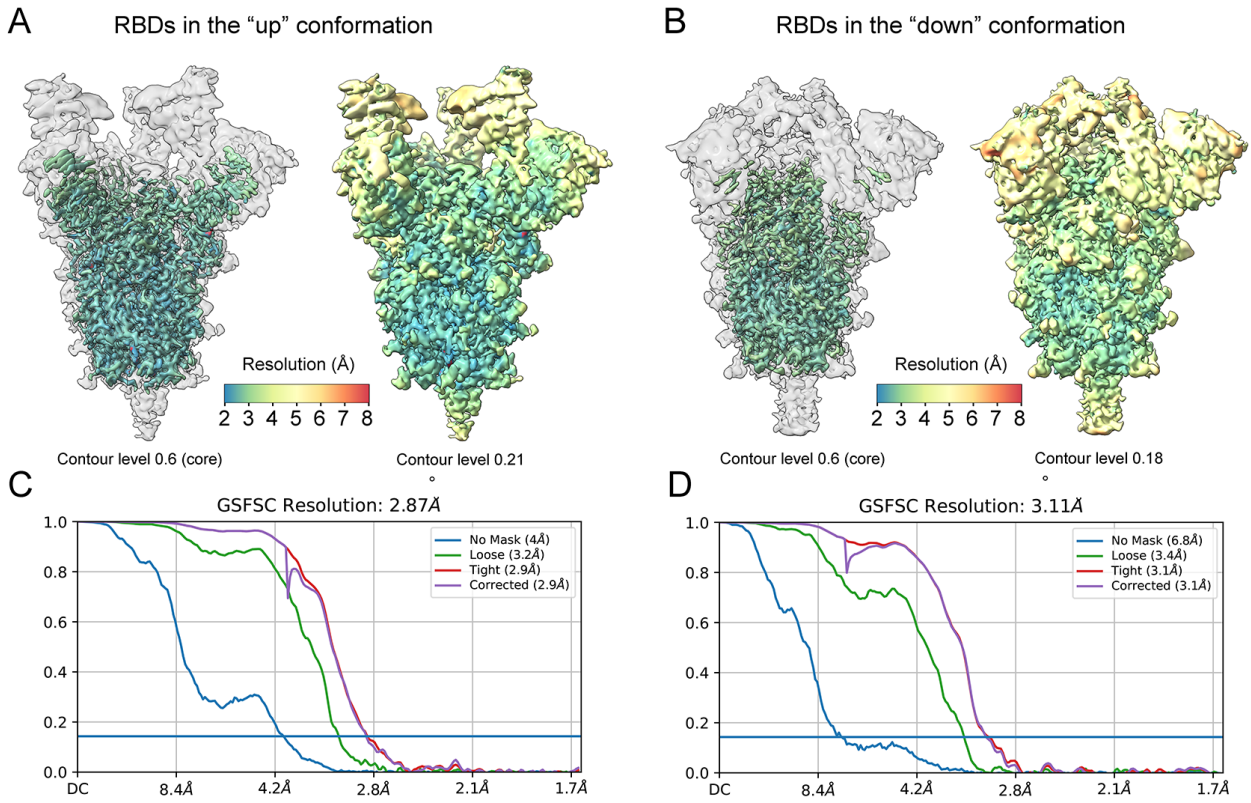

Supplementary Figure 5: CryoEM reconstructions derived from TriSb92-treated SARS-CoV-2 S trimers. Local resolution was estimated and maps were filtered to local resolution in cryoSPARC[1]. **(A)** Reconstruction A describes the S-trimer with all three RBDs in the 'up' conformation, with an average estimated resolution of 2.9 Å, while **(B)** reconstruction B describes the S-trimer with all three RBDs in the 'down' conformation and has average estimated resolution of 3.1 Å. The resolution is highest in the well-ordered S2 subunit, while the intrinsically flexible RBD regions display a more limited resolution. Localized refinement of the RBD regions produced a map at 6.9Å resolution (Fig S6 and S7). **(C-D)** Fourier shell correlation (FSC) plots, calculated between two half-maps as a function of spatial frequency, are shown for reconstructions A and B in panels C and D, respectively.

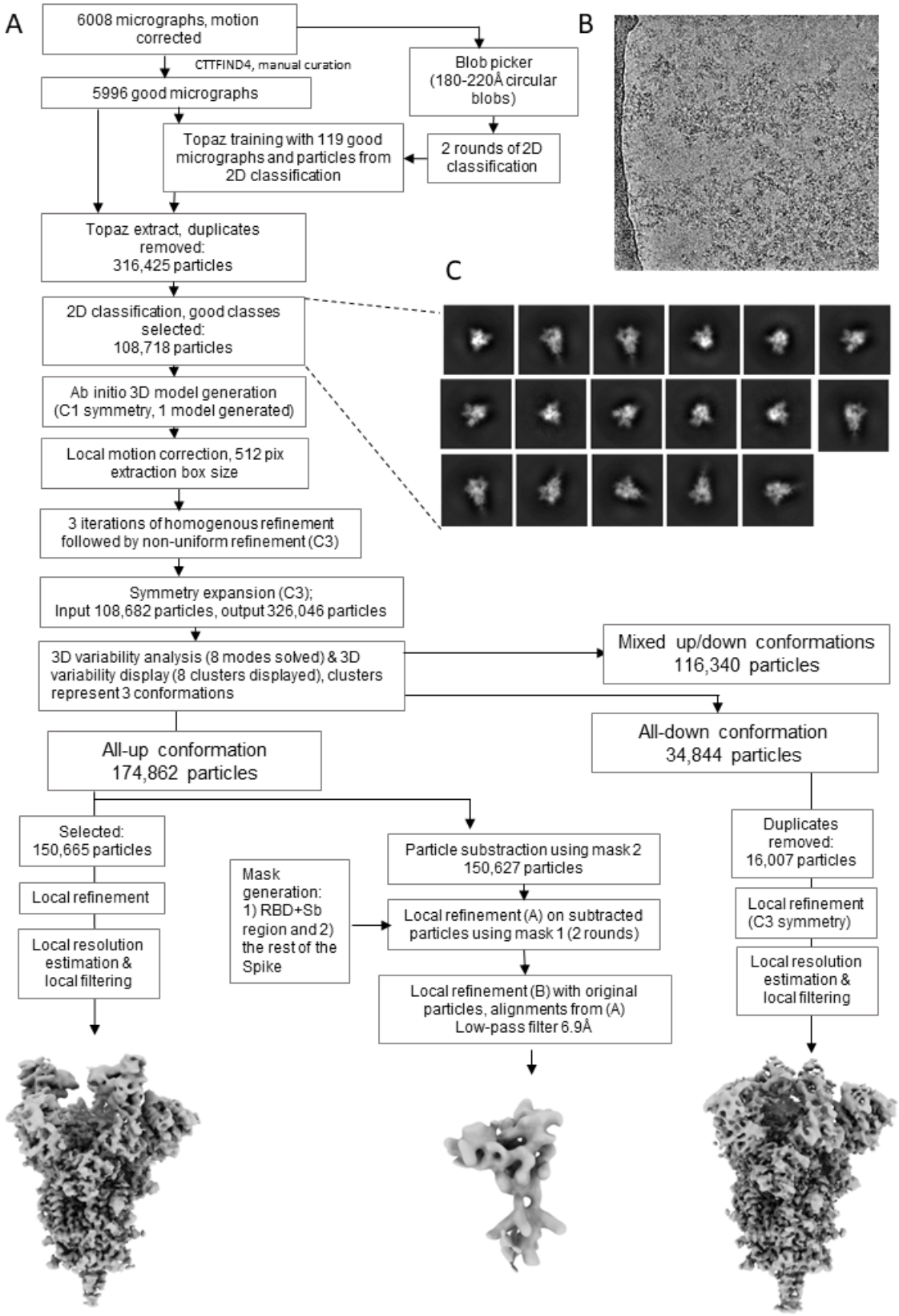

Supplementary Figure 6: CryoEM data processing. (A) Workflow for cryoEM data processing performed in cryoSPARC[1] **(B)** A representative micrograph of TriSb92-treated S trimers. **(C)** 2D classes of the particles selected for ab initio model generation.

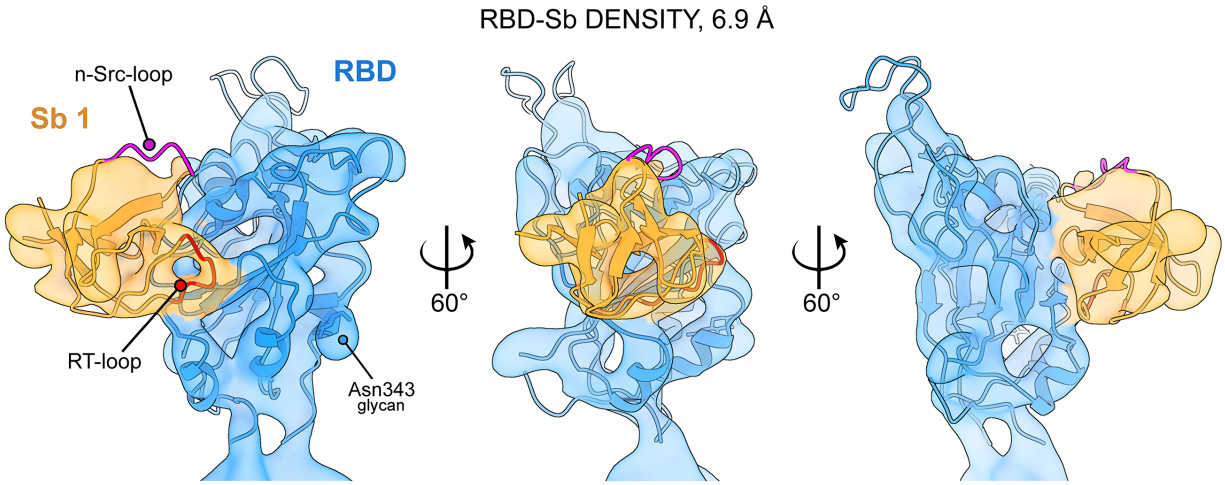

Supplementary Figure 7: Additional density observed in our cryoEM reconstruction matches with the predicted structure of Sb92. Cryo-EM reconstruction of the RBD-TriSb92 complex, with density assigned to the RBD shown in blue, and the density assigned to TriSb92 in orange. The RBD density region is shown with an RBD molecular model (blue, PDB 7A29) and a model of Sb92 (generated with I-TASSER) fitted into the density. The RT- and n-Src loop regions of the SH3 fold that were modified for target-binding specificity (see Fig. 1) are indicated with red and magenta, respectively.

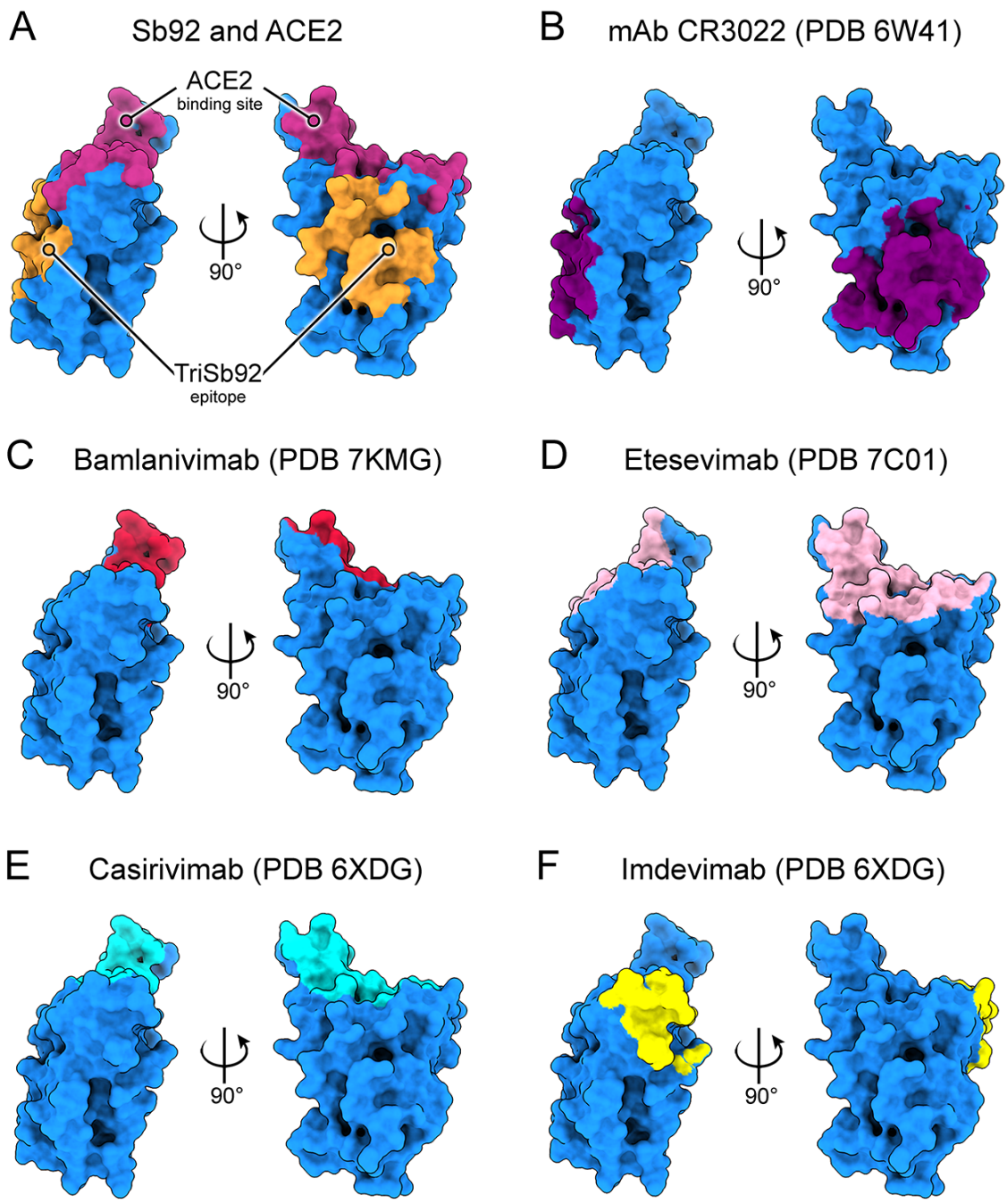

Supplementary Figure 8: Mapping Sb92 epitope in comparison to the epitopes of neutralizing mAbs. A) Sb92 targets an epitope outside of the ACE2-binding region. B) CR3022 (PDB 6W41)[5] a SARS-CoV-1 neutralizer capable of binding the SARS-CoV-2 RBD, utilizes a conserved and cryptic epitope that overlaps with the Sb92 epitope. C), D), E), F) In contrast to Sb92, therapeutic monoclonal antibodies neutralizing SARS-CoV-2 typically target epitopes that overlap with the ACE2 binding site. These include Bamlanivimab (C, PDB 7KMG)[6], Etesevimab (D, PDB 7C01)[7], Casirivimab (E, PDB 6XDG)[8] and Imdevimab (F, PDB 6XDG)[8].

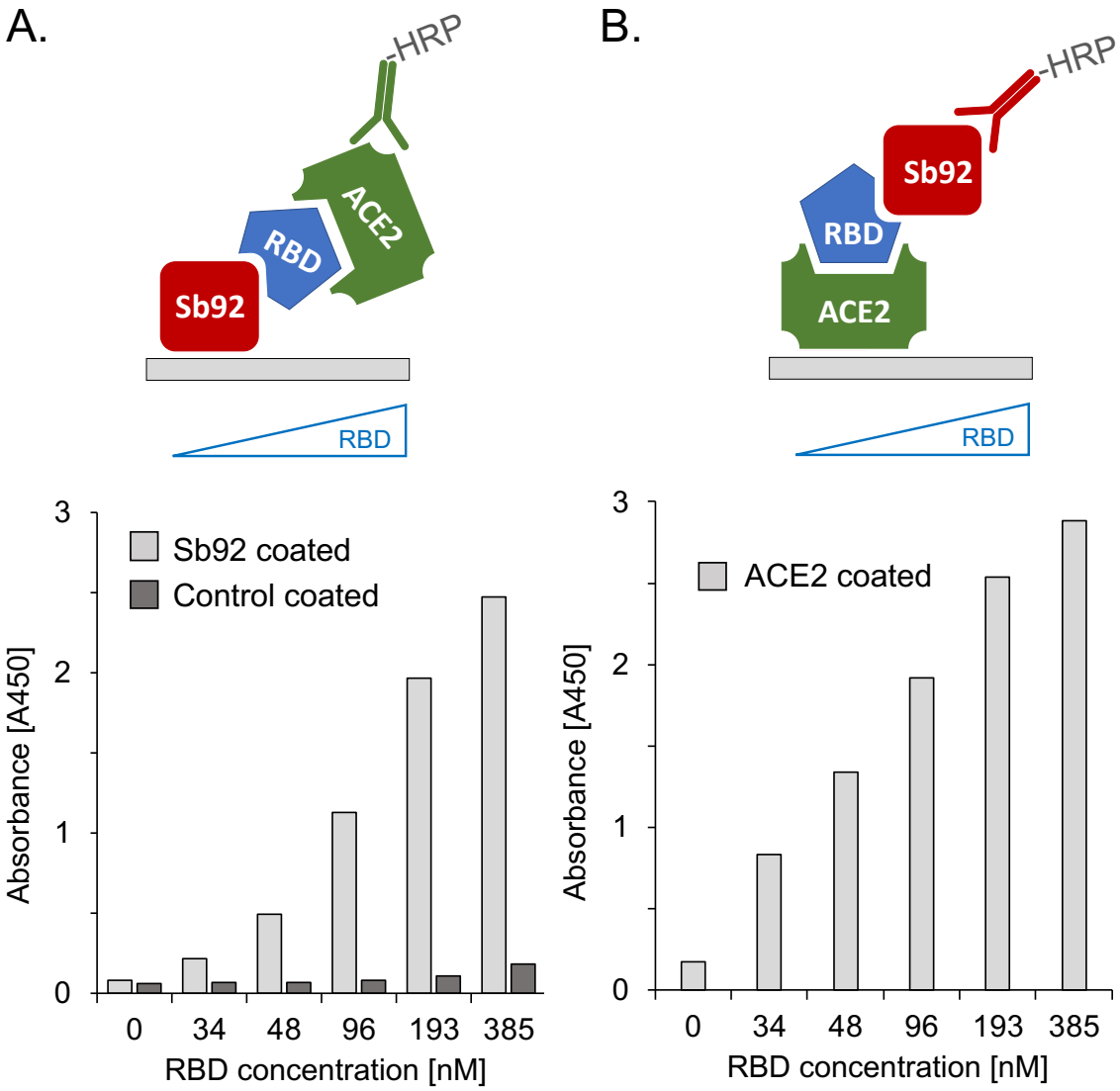

Supplementary Figure 9: Sandwich-ELISAs demonstrating simultaneous binding of Sb92 and ACE2 to RBD. ELISAs were performed in two ways: **(A)** using plastic-coated GST-Sb92 as the capturing reagent and ACE2-mFc as the detector reagent, or **(B)** *vice versa*. In (A) a Her2-specific GST-Sb1206 was also tested as a negative control (Control coated). A constant amount of the capturing and detector reagents were used in each case, while increasing concentrations (0 – 385 nM) of RBD were added as a bridging reagent to test the formation of a trimeric Sb92-RBD-ACE2 complex, which was visualized using a HRP-conjugated antibody against the detector.

871 **Supplementary Table 1. Cryo-EM data collection and processing statistics.**
872

	S-trimer 'all RBDs up' with TriSb92 EMD-25781 PDB 7TAQ	S-trimer 'all RBDs down' EMD-25782 PDB 7TAR
Data collection and processing		
Magnification	165,000x	165,000x
Voltage (kV)	300	300
Electron exposure (e–/Å^2)	55	55
Defocus range (μm)	1.5–3.0	1.5–3.0
Pixel size (Å)	0.82	0.82
Symmetry imposed	C1	C3
Initial particle images (no.)	316,425	316,425
Final particle images (no.)	150,665 (C3 symmetry expanded)	16,007
Map resolution (Å)	2.87	3.11
FSC threshold	0.143	0.143

873

874

875 **Supplementary Table 2. Summary of viral nucleoprotein immunohistochemistry findings in**
876 **the mice included in Experiment 3 of Figure 3A.**
877
878

Animal number	Treatment group	NP immunohistochemistry findings
B22-0089	**Untreated**	**Lungs:** All bronchioles positive, with few to all epithelial cells (EC) positive, viral antigen along luminal surface; next to some bronchioles or widespread patches/areas of alveoli with positive type I and II pneumocytes, and some free viral antigen in lumen. **Trachea**: individual positive EC. **Bronchial lymph node (LN)**: Several positive macrophages/DC
B22-0090	**Untreated**	**Lungs:** Most bronchioles positive, with few to all EC positive, viral antigen along luminal surface; next to some bronchioles or numerous patches/areas of alveoli with positive type I and II pneumocytes, and some free viral antigen in lumen; **Trachea**: Individual positive EC and viral antigen along lumen
B22-0091	**Untreated**	**Lungs:** All bronchioles positive, with few to all EC positive, viral antigen along luminal surface; next to some bronchioles or widespread patches/areas of alveoli with positive type I and II pneumocytes, and some free viral antigen in lumen; **Trachea**: several individual positive EC, some viral antigen in lumen; **Bronchial LN**: several positive macrophages/DC
B22-0092	**Untreated**	**Lungs:** Many bronchioles with few to all EC positive, viral antigen along luminal surface; next to some bronchioles or widespread patches/areas of alveoli with positive type I and II pneumocytes, and some free viral antigen in lumen; **Trachea**: Several individual positive EC, some viral antigen in lumen; **Bronchial LN**: Several positive macrophages/DC
B22-0093	**Untreated**	**Lungs:** All bronchioles positive, with few to all EC positive, viral antigen along luminal surface; next to some bronchioles or widespread patches/areas of alveoli with positive type I and II pneumocytes and some free viral antigen in lumen; **Trachea**: Several individual positive EC, some viral antigen in lumen; **Bronchial LN**: Several positive macrophages/DC.
B22-0094	**- 2h**	**Lungs:** Negative**; Trachea**: Negative; **Bronchial LN:** Negative
B22-0095	**- 2h**	**Lungs:** Negative**; Trachea**: Negative; **Bronchial LN:** Negative
B22-0096	**- 2h**	**Lungs:** Negative**; Trachea**: Negative; **Bronchial LN:** Negative
B22-0097	**- 2h**	**Lungs:** Negative**; Trachea**: Negative; **Bronchial LN:** Negative
B22-0098	**- 2h**	**Lungs:** Negative**; Trachea**: Negative; **Bronchial LN:** Negative
B22-0099	**+ 2h**	**Lungs:** A few bronchioles with small to extensive patches of positive EC, viral antigen along luminal surface; a few small patches of alveoli with positive type I and

		II pneumocytes (mainly intact), also within consolidated areas; **Bronchial LN**: A few positive macrophages/DC
B22-0100	**+ 2h**	**Lungs:** A few individual and small patches of positive EC in bronchioles; a few small patches of alveoli with positive type I and II pneumocytes (intact)
B22-0101	**+ 2h**	**Lungs:** Several bronchioles with small to extensive patches of positive EC, viral antigen along luminal surface; several small to larger patches of alveoli with positive type I and II pneumocytes (mainly intact); **Trachea**: One patch of positive EC; **Bronchial LN**: Negative
B22-0102	**+ 2h**	**Lungs:** Several bronchioles with small to extensive patches of positive EC, some viral antigen along luminal surface; several small patches of alveoli with positive type I and II pneumocytes (mainly intact)
B22-0103	**+ 2h**	**Lungs:** Bronchioles with small to extensive patches of positive EC, viral antigen along luminal surface; several small patches of alveoli with positive type I and II pneumocytes (mainly intact), also within consolidated areas; **Bronchial LN**: A few positive macrophages/DC
B22-0104	**+ 4h**	**Lungs:** Several bronchioles with small to extensive patches of positive EC, viral antigen along luminal surface; several small patches of alveoli with positive type I and II pneumocytes (mainly intact); **Trachea**: Negative; **Bronchial LN**: Negative
B22-0105	**+ 4h**	**Lungs:** A few bronchioles with small to extensive patches of positive EC; a few small patches of alveoli with positive type I and II pneumocytes; **Trachea**: Negative; **Bronchial LN**: Negative
B22-0106	**+ 4h**	**Lungs:** A few bronchioles with small to extensive patches of positive EC and degenerate positive cells in lumen; a few small patches of alveoli with positive type I and II pneumocytes; **Trachea**: Negative
B22-0107	**+ 4h**	**Lungs:** Rare bronchioles with small to larger patches of positive EC; several small patches of alveoli with positive type I and II pneumocytes; **Trachea**: Negative
B22-0108	**+ 4h**	**Lungs:** Rare bronchioles with a few small patches of positive EC; a few small patches of alveoli with positive type I and II pneumocytes; **Trachea**: Negative
B22-0109	**+ 8h**	**Lungs:** Several bronchioles with a few individual to large patches of positive EC; several small patches of alveoli with positive type I and II pneumocytes
B22-0110	**+ 8h**	**Lungs:** A few bronchioles with a few individual to large patches of positive EC; several small patches of alveoli with positive type I and II pneumocytes; **Bronchial LN**: Negative
B22-0111	**+ 8h**	**Lungs:** several bronchioles with a few individual to large patches of positive EC; in one area a few small patches of alveoli with positive type I and II pneumocytes; **Bronchial LN**: Rare positive macrophages/DC
B22-0112	**+ 8h**	**Lungs:** several large bronchioles with many to all EC positive, viral antigen along luminal surface, a few bronchioles with a few individual or very small patches of positive EC; rare patches of alveoli with positive type I and II cells; **Trachea**: several individual positive EC, some viral antigen in lumen; **Bronchial LN**: A few positive macrophages/DC

B22-0113	**+ 8h**	**Lungs:** a few individual positive EC in bronchioles; several random small patches of alveoli with positive type I and II pneumocytes; **Bronchial LN**: Negative

879
880

881 **Supplementary references**

882 1. Punjani, A., Rubinstein, J.L., Fleet, D.J. & Brubaker, M.A. cryoSPARC: algorithms for
883 rapid unsupervised cryo-EM structure determination. *Nat Methods* **14**, 290-296
884 (2017).

885 2. Custodio, T.F. et al. Selection, biophysical and structural analysis of synthetic
886 nanobodies that effectively neutralize SARS-CoV-2. *Nat Commun* **11**, 5588 (2020).

887 3. Xiong, X. et al. A thermostable, closed SARS-CoV-2 spike protein trimer. *Nat Struct*
888 *Mol Biol* **27**, 934-941 (2020).

889 4. le Maire, A. et al. Solution NMR structure of the SH3 domain of human nephrocystin
890 and analysis of a mutation-causing juvenile nephronophthisis. *Proteins* **59**, 347-355
891 (2005).

892 5. Yuan, M. et al. A highly conserved cryptic epitope in the receptor binding domains of
893 SARS-CoV-2 and SARS-CoV. *Science* **368**, 630-633 (2020).

894 6. Jones, B.E. et al. The neutralizing antibody, LY-CoV555, protects against SARS-CoV-2
895 infection in nonhuman primates. *Sci Transl Med* **13** (2021).

896 7. Shi, R. et al. A human neutralizing antibody targets the receptor-binding site of SARS-
897 CoV-2. *Nature* **584**, 120-124 (2020).

898 8. Hansen, J. et al. Studies in humanized mice and convalescent humans yield a SARS-
899 CoV-2 antibody cocktail. *Science* **369**, 1010-1014 (2020).

900